CHANDRA ORION ULTRADEEP PROJECT: OBSERVATIONS AND SOURCE LISTS

K. V. GETMAN,[1] E. FLACCOMIO,[2] P. S. BROOS,[1] N. GROSSO,[3] M. TSUJIMOTO,[1] L. TOWNSLEY,[1] G. P. GARMIRE,[1]
J. KASTNER,[4] J. LI,[4] F. R. HARNDEN, JR.,[5] S. WOLK,[5] S. S. MURRAY,[5] C. J. LADA,[5] A. A. MUENCH,[5]
M. J. MCCAUGHREAN,[6,7] G. MEEUS,[7] F. DAMIANI,[2] G. MICELA,[2] S. SCIORTINO,[2] J. BALLY,[8]
L. A. HILLENBRAND,[9] W. HERBST,[10] T. PREIBISCH,[11] AND E. D. FEIGELSON[1]

ABSTRACT

We present a description of the data reduction methods and the derived catalog of more than 1600 X-ray point sources from the exceptionally deep 2003 January *Chandra X-Ray Observatory* (*Chandra*) observation of the Orion Nebula Cluster and embedded populations around OMC-1. The observation was obtained with *Chandra*'s Advanced CCD Imaging Spectrometer (ACIS) and has been nicknamed the *Chandra* Orion Ultradeep Project (COUP). With an 838 ks exposure made over a continuous period of 13.2 days, the COUP observation provides the most uniform and comprehensive data set on the X-ray emission of normal stars ever obtained in the history of X-ray astronomy.

Subject headings: ISM: individual (Orion Nebula, OMC-1) — open clusters and associations:
                    individual (Orion Nebula Cluster) — stars: early-type — stars: pre–main-sequence —
                    X-rays: stars

Online material: extended figure set, machine-readable tables

1. INTRODUCTION

The processes of star formation and early stellar evolution have proved to be complex in many respects. Gravitational collapse can be hindered by magnetic and turbulent pressures and is accompanied by collimated jets and outflows during the protostellar phase. The dynamics and evolution of circumstellar disks where planets form are still under study. The birth of stars rarely occurs in isolation. Most stars form in a hierarchy ranging from binaries to rich clusters. These processes, which take place in thermodynamically cold and neutral media with characteristic energies of $\ll 1$ eV per particle, paradoxically produce and are subject to violent high-energy processes with characteristic energies of $\gtrsim 10^3$ eV. The principal evidence for this is X-ray emission (and sometimes nonthermal radio emission) from stars throughout their pre–main-sequence (PMS) evolution (Feigelson & Montmerle 1999).

PMS X-ray emission is elevated from 10^1 to $\gtrsim 10^4$ times above typical main-sequence levels for stars with masses $0.1\ M_\odot \lesssim M \lesssim 2\ M_\odot$. High-amplitude X-ray variability and hard spectra, supported by multiwavelength studies such as photospheric Zeeman measurements and starspot mapping, indicate that the emission is primarily attributable to solar-type magnetic flares where plasma is heated to high temperatures by violent reconnection events in magnetic loops. However, the empirical relationships between PMS X-ray emission and stellar age, mass, radius, and rotation differ from those seen among solar-type main-sequence stars (Flaccomio et al. 2003b; Feigelson et al. 2003). We have an inadequate understanding of the astrophysical origins of this magnetic activity. It is also unclear whether or not the high-energy radiation from magnetic flaring has important astrophysical effects. For example, it is possible that some planets form in disk regions that are rendered turbulent from MHD instabilities induced by PMS X-rays (e.g., Glassgold et al. 2000; Matsumura & Pudritz 2003). X-rays from embedded stars may affect ambipolar diffusion, and thus future star formation, in the surrounding molecular cloud. X-ray images are also particularly effective in locating low-mass companions around luminous young stars. There are thus a variety of astrophysical reasons to investigate the magnetic activity of young stars. Due to the wide range of activity levels and other properties, it is advantageous to study large samples of stars.

The nearest rich and concentrated sample of PMS stars is the Orion Nebula Cluster (ONC), also known as the Trapezium Cluster or Ori Id OB association. The OB members of the ONC illuminate the Orion Nebula (=M42), a blister H II region at the near edge of Orion A, the nearest giant molecular cloud ($D \simeq 450$ pc). The ONC has $\simeq 2000$ members within a 1 pc ($8'$) radius sphere, with 80% of the stars younger than 1 Myr (Hillenbrand 1997). It was the first young stellar cluster to be detected in the X-ray band (Giacconi et al. 1972), and nonimaging studies soon found that the X-ray emission is extended on scales of a parsec or larger (den Boggende et al. 1978; Bradt & Kelley 1979). Early explanations for the Orion X-rays included winds from the massive Trapezium stars colliding with each other or the molecular cloud, and hot coronae or magnetic activity in lower mass T Tauri stars. The *Einstein* (Ku & Chanan 1979), *Röntgensatellit* (*ROSAT*; Gagné et al. 1995; Geier et al. 1995; Alcalá et al. 1996), and the *Advanced Satellite for Cosmology and Astrophysics* (*ASCA*; Yamauchi et al. 1996) imaging X-ray observatories established that both the Trapezium stars and many lower mass T Tauri stars contribute to the X-ray emission.

[1] Department of Astronomy and Astrophysics, Pennsylvania State University, 525 Davey Laboratory, University Park, PA 16802.
[2] INAF, Osservatorio Astronomico di Palermo G. S. Vaiana, Piazza del Parlamento 1, I-90134 Palermo, Italy.
[3] Laboratoire d'Astrophysique de Grenoble, Universite Joseph Fourier, BP 53, 38041 Grenoble Cedex 9, France.
[4] Chester F. Carlson Center for Imaging Science, Rochester Institute of Technology, 54 Lomb Memorial Drive, Rochester, NY 14623.
[5] Smithsonian Astrophysical Observatory, 60 Garden Street, Cambridge, MA 02138.
[6] University of Exeter, School of Physics, Stocker Road, Exeter EX4 4QL, Devon, UK.
[7] Astrophysikalisches Institut Potsdam, An der Sternwarte 16, D-14482 Potsdam, Germany.
[8] Center for Astrophysics and Space Astronomy, University of Colorado at Boulder, CB 389, Boulder, CO 80309.
[9] Department of Astronomy, California Institute of Technology, 1200 East California Boulevard, Pasadena, CA 91125.
[10] Max-Planck-Institut fur Astronomie, Konigstuhl 17, D-69117 Heidelberg, Germany.
[11] Max-Planck-Institut fur Radioastronomie, Auf dem Hugel 69, D-53121 Bonn, Germany.

TABLE 1
COUP Observations

ObsID	Start Time	Exposure (ks)	R.A. (J2000.0) (deg)	Decl. (J2000.0) (deg)	Roll Angle (deg)
4395....................	2003 Jan 8 20:58:18.8	99.9	83.8210052	−5.394400	310.90882
3744....................	2003 Jan 10 16:17:38.7	164.2	83.8210086	−5.394406	310.90882
4373....................	2003 Jan 13 07:34:43.5	171.5	83.8210098	−5.394403	310.90882
4374....................	2003 Jan 16 00:00:37.4	168.9	83.8210079	−5.394404	310.90882
4396....................	2003 Jan 18 14:34:48.3	164.5	83.8210094	−5.394403	310.90882
3498....................	2003 Jan 21 06:10:27.7	69.1	83.8210025	−5.394402	310.90882

Notes.—ObsID values are from the *Chandra* Observation Catalog. Start times are in UT. Exposure times are the sum of Good Time Intervals (GTIs) for the CCD at the telescope aim point (CCD3) minus 1.3% to account for CCD readouts. The aim points and roll angles are obtained from the satellite aspect solution before astrometric correction was applied.

But these early studies could detect only a modest fraction of the ONC stars due to the high stellar densities and heavy absorption by molecular material along the line of sight. These limitations are alleviated by NASA's *Chandra X-Ray Observatory* (*Chandra*). Its mirrors provide an unprecedented combination of capabilities—a wide spectral bandpass and $\lesssim 1''$ spatial resolution—and are particularly well-suited to the study of crowded and absorbed clusters of faint X-ray sources. The ONC was thus intensively studied during the first year of the *Chandra* mission with several instrumental setups: the Advanced CCD Imaging Spectrometer (ACIS) in imaging mode (Garmire et al. 2000; Feigelson et al. 2002a, 2002b, 2003) and as detector for the High Energy Transmission Grating Spectrometer (Schulz et al. 2000, 2001, 2003), and with the High Resolution Imager (HRI; Flaccomio et al. 2003a, 2003b).

While many valuable results emerged from these early *Chandra* studies, it was recognized that more would be learned from a much deeper and longer exposure of the Orion Nebula region. We present here a unique ∼10 day, nearly continuous observation of the Orion Nebula obtained during the fourth year of the mission, nicknamed the *Chandra* Orion Ultradeep Project (COUP).[12] This paper describes the COUP observations (§ 2), the data reduction (§ 3), source detection and characterization (§§ 4–9), and identification with previously known PMS stars (§§ 10–11). We provide extensive machine-readable tables of the X-ray sources and properties, and an atlas of their location in the sky (§ 12). Other COUP papers will discuss various astronomical and astrophysical issues emerging from these observations.

2. OBSERVATIONS

The COUP combines six nearly consecutive exposures of the Orion Nebula Cluster (ONC) spanning 13.2 days in 2003 January with a total exposure time of 838 ks or 9.7 days (Table 1). The observations were obtained with the ACIS camera on board *Chandra*, which are described by Weisskopf et al. (2002) and Garmire et al. (2003). We consider here only results arising from the imaging array (ACIS-I) of four abutted 1024×1024 pixel front-side–illuminated charge-coupled devices (CCDs) covering about $17' \times 17'$ on the sky. The S2 chip in the spectroscopic array (ACIS-S) was also operational, but as the telescope point-spread function (PSF) is considerably degraded far off-axis, the S2 data are omitted from the analysis. The ACIS-I aim point and the roll angle for all six observations were kept constant (Table 1). All six observations were taken in Very Faint telemetry mode to improve the screening of background events and thus increase the sensitivity of the observations. The focal plane temperature was between −119.5 and −119.7°C.

The observations were constrained to be performed in January to accommodate a single roll of about 311°. The observational span of 14 days means that the spacecraft's nominal roll changes by about 14°. Typically, off-nominal rolls of greater than ±5° are difficult to accommodate. However, in January of 2003 the tolerance was somewhat higher in the direction of the ONC. The observations were continuous with the exception of five passages through the Van Allen belts, during each of which ACIS is taken out of the focal plane for about 29 ks. The spacecraft used these passages to unload momentum so that no other science target was observed between 2003 January 8 21:00 GMT and 2003 January 22 02:00 GMT. The outcome of 9.7 days exposure in a 13.2 day period (73% efficiency) is the maximum efficiency achievable by the spacecraft given the current perigee of about 33,000 km.

The COUP observation period was also remarkable in having some of the quietest solar weather in the *Chandra* mission. This reduces instrumental background and makes the data set truly exceptional for variability analysis. The *Advanced Composition Explorer* spacecraft, which is used to monitor the solar wind near the Earth, never saw fluxes above 200 particles cm^{-2} s^{-1} sr^{-1} MeV^{-1} in the P3 channel (112–187 keV). *Chandra* observations are generally terminated when this rate exceeds 50,000 to prevent damage to the ACIS CCDs. All particle detectors associated with the on-board Electron Proton Helium Instrument (EPHIN) also reported some of their lowest background measurements during this period. Nonetheless, some data were lost. The typical ONC observation included about 45,000 frames (3.2 s exposures) from each of the five CCDs. Typically, less than 10 frames (20 events) from each CCD were lost due to telemetry errors. However, the final observation, ObsID 3498, lost about 40 frames (∼80 events) of the roughly 18,000 sent from each CCD.

3. DATA SELECTION

The COUP data reduction and cataloging procedure is diagrammed in Figure 1. We outline in this section the first steps of data selection; see Appendix B of Townsley et al. (2003) for more details on many of these steps. Procedures were performed with CIAO software package version 2.3, FTOOLS version 5.2, XSPEC version 11.2, the Penn State CTI corrector version 1.16, and the `acis_extract` package version 2.33. The latter two tools were developed at Penn State.[13]

---

[12] Links to the COUP data set are available in the electronic edition of the *Supplement*.

[13] Descriptions and codes for CTI correction and `acis_extract` can be found at http://www.astro.psu.edu/users/townsley/cti/ and http://www.astro.psu.edu/xray/docs/TARA/ae_users_guide.html, respectively.

For each of 6 obsids.

Filter CXC evt1 files on 4 CCDs; mark bg. in VF mode; apply PSU CTI correction; apply grade, status, GTI, hot pixel, and coarse energy filtering.

Cross-identify bright X-ray sources with VLT catalog; improve absolute astrometry; remove position randomization.

Combine all obsids, create combined exposure map.

Remove flaring pixels.

Apply subpixel event relocation (SER).

Clean bg. in VF mode.

Perform Bayesian Blocks analysis.

Extract source data with acis_extract (AE).

Detect sources with WDetect.

Detect sources with PWDetect.

Produce final COUP sourcelist.

Extraction files, including spectra, lightcurves, Bayesian Blocks, PSF images, smoothed data images, and many more.

Produce 7 tables recording information with X-ray source lists and positions, variability, photometry, spectra, luminosity, IR and optical properties.

Cross-identify COUP sources with objects from optical and IR catalogs.

Estimate count rates of undetected sources with PWDetect.

Produce the atlas in PDF format, summarizing each source in one page.

Produce 3 tables for sources, undetected by COUP.

Deliver the reduced data and tables to science groups.

Fig. 1.—Diagram of the COUP data reduction and catalog procedure.

Data reduction starts with Level 1 event files provided by the *Chandra* X-Ray Center (CXC). First, we filter out events on the S2 chip. Second, likely cosmic-ray and associated afterglow events are identified, but not removed, by taking advantage of the Very Faint telemetry mode. Third, employing the PSU CTI Corrector (Townsley et al. 2002), the data are partially corrected for CCD charge transfer inefficiency (CTI) caused mainly by radiation damage at the beginning of the *Chandra* mission. Fourth, the data are cleaned with filters on event "grade" (only *ASCA* grades 0, 2, 3, 4, and 6 are accepted), "status," and "good-time interval" filters supplied by the CXC. Energies <500 eV and background events with energies >10,500 eV are removed. Bad pixel columns with energies <700 eV, left by the standard processing, are removed. Fifth, for each of the six COUP observations, individual correction to the absolute astrometry was applied based on several hundred matches between the preliminary *Chandra* and Very Large Telescope (VLT) point source catalogs (see § 10). Along with reapplying the new aspect solutions to the data lists, the slight broadening of the PSF from the CXC's software randomization of positions was removed. Sixth, the tangent planes (x, y coordinate systems) of the five COUP observations were reprojected to match the tangent plane of the first observation (ObsID 4395), and all six files were merged into a single data event file.

For the purpose of source detection only, we eliminated flaring pixel events and events identified earlier using Very Faint mode that, when combined with random background events, can produce faint spurious sources. This cleaning operation reduced the background by ~17%, but at the same time it removed ~7% of real photons from many bright sources. In the later source photon extraction stage (see Fig. 1), we use an event list that retains these events so that source brightnesses are not underestimated.

Figure 2 shows the resulting images. Note the bright CCD readout streaks emanating from the brightest sources. In actuality, every source in the field produces similar readout streaks, producing a spatially variable background that must be considered when sources are detected. The chip gaps and bad pixel columns in the form of white stripes are also noticeable, as the images displayed here have not been corrected for the exposure map.

As a large fraction of PMS stars are expected to be in binary systems, some with separations comparable to the *Chandra* PSF, we have applied a subpixel event repositioning (SER) technique to improve the effective resolution of the ACIS detector. The SER procedure used here considers the "splitting" of charge between adjacent CCD pixels in an energy-dependent fashion (Li et al. 2004). We have applied SER to the merged exposure with cosmic-ray afterglow events removed. We tested the results of SER by examining image quality for 100 COUP sources with >300 counts
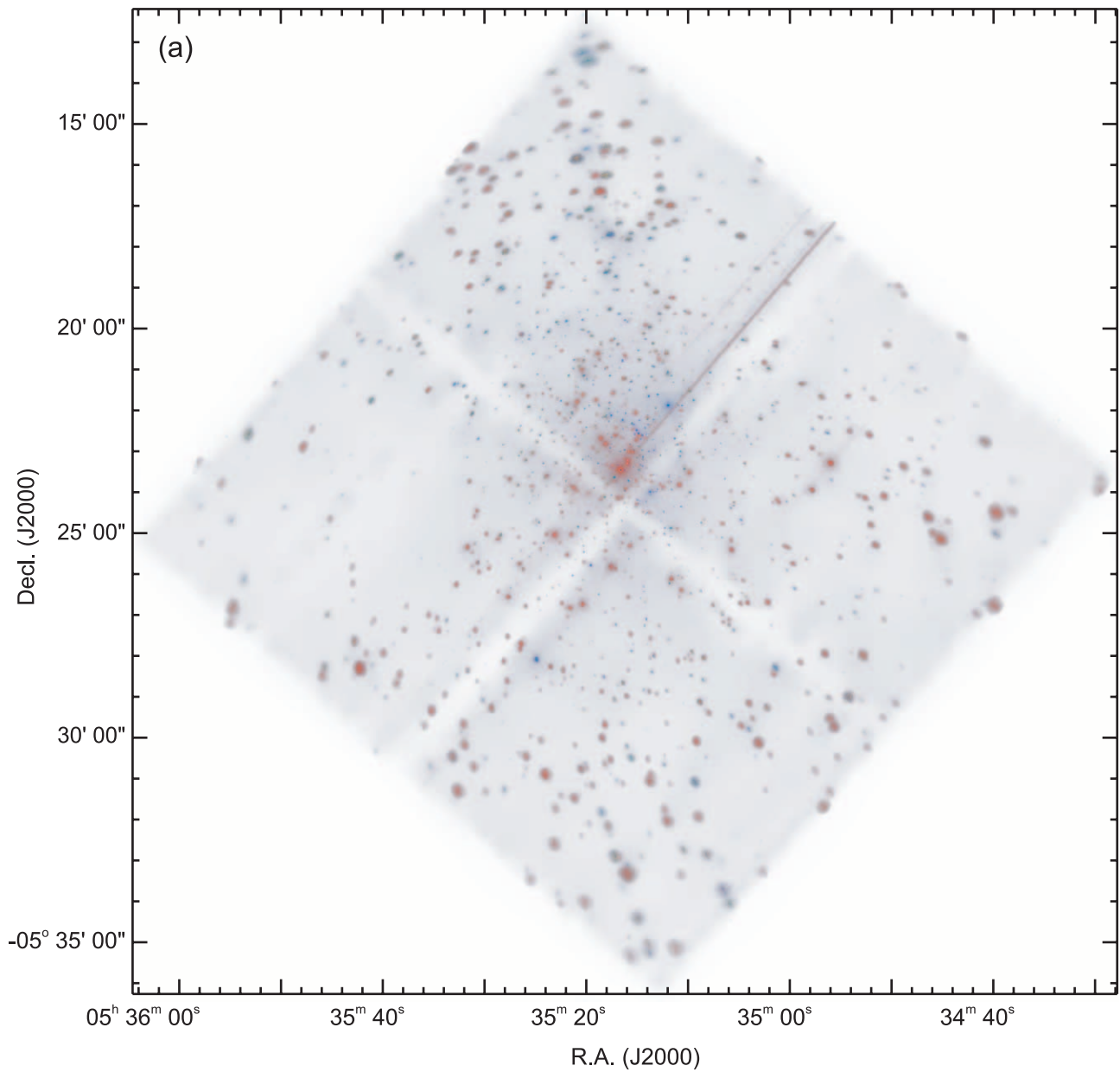
Fig. 2.—COUP ACIS-I image: (*a*) the full ACIS-I field shown with 1″ pixels, and (*b*) the central region (4′ × 4′) shown with 0″.25 pixels. The image is shown after adaptive smoothing. The energy of each pixel is coded in color so that soft (0.5–1.7 keV) (unabsorbed) sources appear red, while hard (2.8–8.0 keV), often absorbed, sources appear blue. Green indicates moderately absorbed sources with typical energies of 1.7–2.8 keV. Brightness is scaled to the logarithm of the photon number in the displayed pixel. The color model depicts zero flux as white. Images are not corrected for the exposure map and thus show gaps between the four CCD chips.
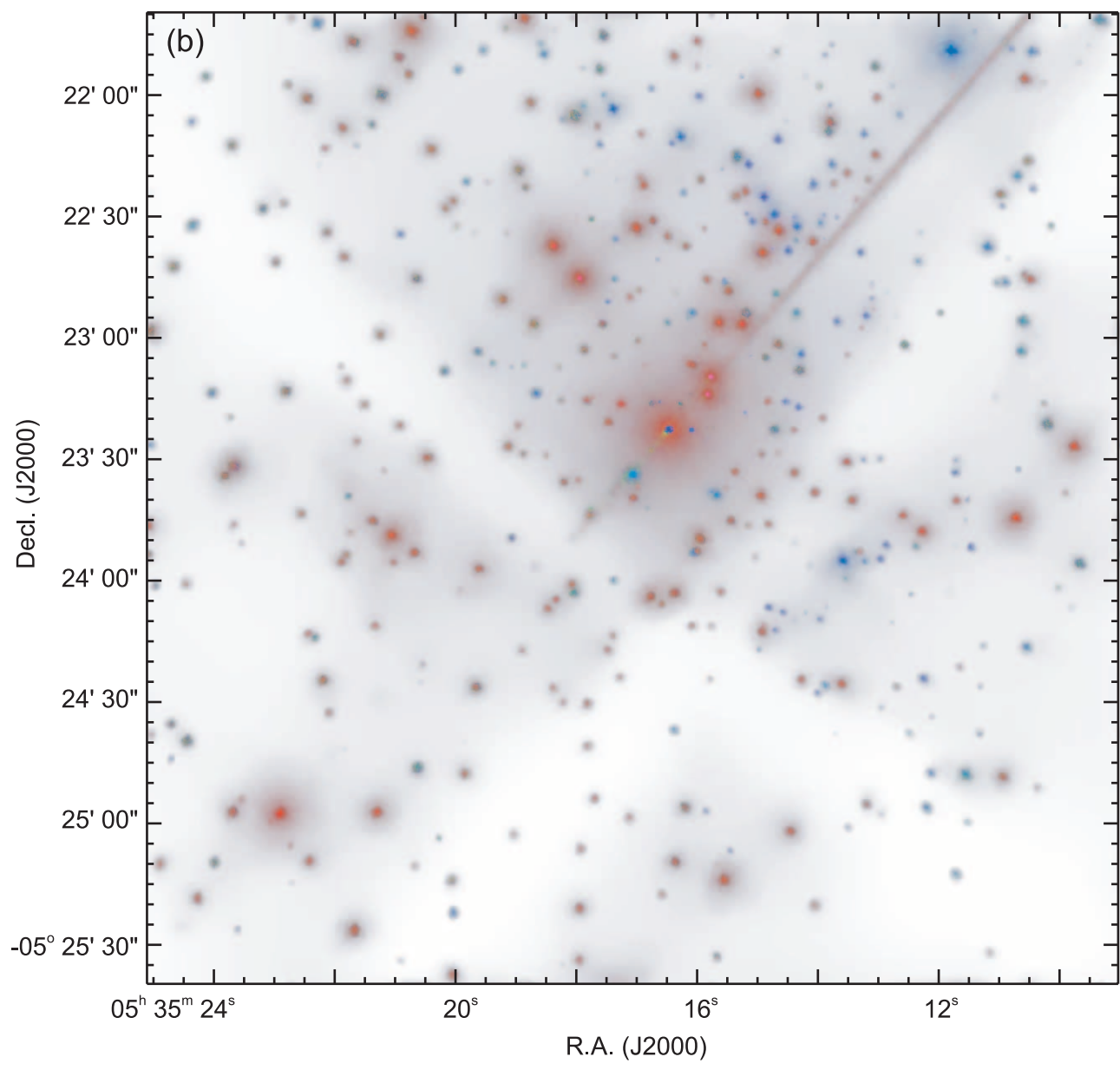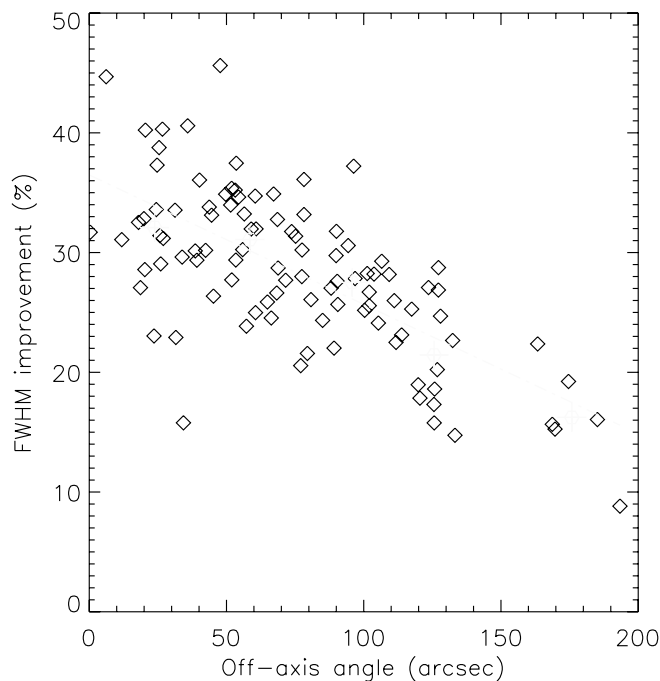
Fig. 2.—*Continued*

Fig. 3.—Improvement in the FWHM width of the PSF of 100 COUP sources due to application of the subpixel repositioning (SER) procedure.

located at off-axis angles $\theta \lesssim 3'$. A 36% improvement in the PSF FWHM is achieved on-axis. As expected from the PSF broadening off-axis, the SER-induced improvement decreases to 31%, 21%, and 16% at $\theta = 1'$, $2'$, and $3'$ off-axis, respectively (see Fig. 3).

4. SOURCE DETECTION

As there is no single optimal procedure for identifying sources in such a rich *Chandra* field, trial source lists were prepared independently by two groups within the COUP team. The Penn State group used a wavelet transform detection algorithm implemented as the `wavdetect` program within the CIAO data analysis system (Freeman et al. 2002). The Palermo group used the Palermo wavelet transform detection code, PWDetect.[14] Source detection procedures were carried out on both the original and SER-corrected images and on images constrained to include only soft and only hard events.

4.1. *Penn State Procedure*

A *Chandra* imaging effective exposure map with units of cm^2 s counts photons^{-1} was made from the product of an aspect histogram `asphist` and an instrument map. The aspect histogram gives the amount of time the *Chandra* optical axis dwelled on each part of the sky and is derived from the satellite aspect solution. The instrument map provides the instantaneous effective area across the field of view. It includes the detector quantum efficiency, nonuniformities across the face of a detector, mirror vignetting, and bad pixels.

To reduce unnecessary computation on high-resolution images far off-axis where the PSF is degraded, we constructed four 1024×1024 pixel scenes around the aim point with $0\rlap{.}''25$, $0\rlap{.}''50$, $1\rlap{.}''00$, and $1\rlap{.}''44$ pixels. An effective exposure map was created

for each scene assuming a monochromatic incident spectrum with photon energy of 1.6 keV, the approximate energy at which the largest number of photons was detected. To improve sensitivity to faint sources with unusually soft or hard spectra, for each scene we produced energy band–limited images from the merged event list (cleaned of flaring events) in the total band (0.5–8.0 keV), soft band (0.5–2.0 keV), and hard band (2.0–8.0 keV). These images were produced from the original merged event list for the event list with background removal based on Very Faint telemetry mode and for the SER-corrected event list. Source detection was thus performed on 36 1024×1024 images: three event lists, four spatial resolutions, and three spectral bands.

We ran `wavdetect` with the probability threshold $P = 10^{-6}$, which theoretically permits a few false positive detections in each image, and with $P = 10^{-5}$, which permits dozens of false positives. The wavelet scales were set between 1–2, 1–4, 1–8, and 1–16 pixels for the $0\rlap{.}''25$, $0\rlap{.}''50$, $1\rlap{.}''00$, and $1\rlap{.}''44$ scenes, respectively. We then merged the catalogs, keeping only a single entry for each source by removing duplicate entries obtained from detections in lower resolution images, if such entries existed. The sources were then visually examined, resulting in the rejection of 184 `wavdetect` sources. Most of these were spurious triggers lying on the readout trails or PSF wings of θ^1C Ori or other very bright sources. The remainder appear to be random associations of events that did not resemble the local PSF. During this examination of the image 109 closely spaced and weak but likely sources were added to the PSU source list. The resulting combined and cleaned `wavdetect` source list has 1622 detections.

4.2. *Palermo Procedure*

PWDetect is the *Chandra* version of `wdetect`, a source detection code originally developed for *ROSAT* PSPC data, based on wavelet transforms (Damiani et al. 1997a, 1997b). It works directly on event files, instead of binned images, and computes wavelet transforms on a range of spatial scales, to be sensitive to pointlike as well as moderately extended sources. Compared to the *ROSAT* version, the code has been improved in order to deal with *Chandra*'s extremely good spatial resolution, which implies a very sparse distribution of background counts around a source. This Poisson character of the background was taken into account in establishing the detection significance, using empirical formulae based on simulations as described in Damiani et al. (1997a). In the special case of COUP data, PWDetect was further refined to deal with the very large number of events, and, more importantly, with the presence of readout trails and conspicuous PSF wings, both highlighted by the presence of bright sources and responsible for scores of spurious detections if not accounted for. Readout trails are now automatically identified and statistically removed prior to detection, thus greatly reducing the number of spurious detections. The wings of bright sources are treated by suitably raising the detection threshold along the PSF wings. In this way, we are able to discriminate real from false detections even very close to the bright Trapezium stars.

For the COUP analysis, PWDetect was run on the merged event file restricted to events with energies between 300 and 7000 eV (the method was not applied separately to hard and soft bands) and after application of the VF-mode background filtering. The significance threshold was set at 5.0 σ. This number is not strictly the same as the signal-to-noise ratio but is defined as the probability of source existence, expressed in Gaussian sigmas. Simulation of source-free background fields indicate that, at the chosen 5.0 σ significance level, $\approx$10 spurious sources should be present due to Poissonian fluctuations. This is a good compromise: setting the threshold more conservatively at 5.5 σ,

---

[14] Description and code for PWDetect are available at http://www.astropa .unipa.it/progetti_ricerca/PWDetect. For the COUP analysis, the code was modified to accommodate the large number of events, the conspicuous PSF wings due to bright sources, and events occurring during CCD readouts.

TABLE 2
COUP X-Ray Source Locations

Source		Position				Detection					Previous	
Sequence Number (1)	COUP J (2)	R.A. (J2000.0) (deg) (3)	Decl. (J2000.0) (deg) (4)	Err. (arcsec) (5)	θ (arcmin) (6)	Flag 1 (7)	Flag 2 (8)	Flag 3 (9)	Signif. A_E (10)	Signif. PWD. (11)	ACIS Number (12)	HRC Number (13)
1............................	053429.4−052337	83.622730	−5.393730	0.16	11.85	0d000x	11	110	23.9	36.0	...	...
2............................	053429.5−052354	83.623040	−5.398490	0.11	11.83	0d000x	11	110	41.0	94.4	...	10
3............................	053433.9−052211	83.641473	−5.369767	0.59	10.83	00000x	10	100	0.6	...	...	...
4............................	053434.9−052507	83.645653	−5.418817	0.38	10.58	00000x	10	100	0.5	...	...	...
5............................	053438.2−052338	83.659339	−5.393952	0.35	9.66	000000	11	110	4.0	7.0	...	...
6............................	053438.2−052423	83.659281	−5.406534	0.09	9.69	0000w0	11	110	28.8	77.3	2	...
7............................	053439.7−052425	83.665798	−5.407138	0.01	9.30	00p000	11	110	198.6	452.7	4	18
8............................	053439.8−052456	83.665915	−5.415641	0.12	9.35	0000w0	11	110	24.3	54.9	3	...
9............................	053439.9−052642	83.666336	−5.445000	0.04	9.73	0d000x	11	110	123.3	239.6	6	20
10..........................	053440.0−052604	83.666807	−5.434478	0.30	9.52	0d0000	11	110	4.0	11.7	...	...
11..........................	053440.8−052242	83.670374	−5.378408	0.04	9.05	00000x	11	110	72.7	160.8	9	21
12..........................	053440.8−052639	83.670220	−5.444250	0.18	9.49	0d000x	10	002	15.4	...	7	...
13..........................	053440.9−052559	83.670779	−5.433305	0.33	9.27	0d0000	11	110	1.8	6.7	8	...
14..........................	053441.6−052357	83.673450	−5.399378	0.24	8.82	0000wx	11	110	7.7	18.9	...	...
15..........................	053441.7−052652	83.673936	−5.448017	0.12	9.36	0d000x	11	110	25.3	64.9	10	...

Notes.—See § 4.3 for description of the columns. Table 2 is available in its entirety in the electronic edition of the *Astrophysical Journal Supplement*. A portion is shown here for guidance regarding its form and content.

corresponding to ≈1 spurious detection, would result in detecting about 50 fewer sources, with a net loss of ≈40 real sources.

Our initial list of PWDetect sources for the original event list contained 1497 COUP sources. From visual examination, 62 sources were rejected along readout trails, 5 were rejected in the PSF wings of θ^1C Ori, and 7 were flagged as tentative due to their weakness. Fifteen additional sources were clearly visible by eye but were missed by PWDetect due to proximity to other sources. This particularly occurs when two close sources far off-axis, where the PSF is elongated, mimic a single radially symmetric source. The same procedure applied to the SER-corrected event file produced an initial list of 1493 sources. Seven of these were deemed legitimate new sources and were added to the list. The final Palermo source list comprises 1452 detected sources.

4.3. *Final COUP Source List*

From 64 sources detected by wavdetect but undetected by PWDetect, 38 have significance greater than 5.0 σ (i.e., the significance threshold for PWDetect). Of those 38, 19 are double sources, and another 19 are located at the regions of the inhomogeneous exposure map (i.e., chip gaps, field edges, and bad pixel columns). The Palermo procedure emerged with 10 sources missed by the Penn State procedure, so the combined list has 1632 detections. Following photon extraction and local background determination for each source (§ 5), 16 of these sources were found to have <3 net (i.e., background-subtracted) counts. We subjectively decided that such weak sources are unreliable and have placed them in a separate list of tentative sources. The resulting COUP source list of 1616 sources is presented in Table 2.

The column entries to Table 2 are as follows. Column (1) gives the running source number, which will be used in this and other COUP papers. Sources are listed in order of right ascension. Column (2) gives the source name in IAU format (Jhhmmss.s−ddmmss) with the IAU designation COUP J (*Chandra* Orion Ultradeep Project J2000). Columns (3) and (4) give the source position for epoch J2000.0 in degrees. For sources with $\theta < 5'$, the positions are obtained from a simple centroiding algorithm within the acis_extract procedure. For sources located farther off-axis, the wavelet positions were improved by correlating the event distribution with PSF images using a matched-filter technique implemented by acis_extract. Column (5) gives each source's positional uncertainty in arcseconds. These are calculated within acis_extract as 68% (1 σ) confidence intervals using the Student's *T*-distribution.[15] Column (6) gives the off-axis angle for each source in arcminutes.

Column (7) gives a flag indicating a variety of warnings and difficulties. A "u" denotes uncertain objects; these are very weak sources without stellar counterparts that satisfy the detection criteria but are subjectively not completely convincing. Seventy-four sources have "u" designations. A "d" refers to a double source, defined as two sources with overlapping 90% PSF contours. A "p" defines a possible piled-up source, when the surface brightness of the source exceeds a level of 0.003 counts s^{-1} pixel^{-1}. A "t" indicates that a source region crosses a bright source readout trail. A "w" indicates that the source is located in the wings of any bright source with number of counts >20,000. An "x" indicates a region of inhomogeneous or low exposure map, where the source is located near or on chip gaps, bad pixel columns, or field edges. Sources designated "x" will have disturbed light curves.

---

[15] The Central Limit Theorem (see, e.g., Lyons 1993, p. 17) says that the mean values of all possible samples of a given size N drawn from a particular population tend to cluster in a bell-shaped curve (like Gaussian) around the mean of the population from which the samples are drawn, and the standard deviation of such a set of sample means ($\sigma_{\bar{x}}$) is related to the standard deviation of the population (σ) as $\sigma_{\bar{x}} = \sigma/\sqrt{N}$. The positions of N events extracted from the source region may be considered as a sample of size N out of the set of all possible samples of that size drawn from the parent population (i.e., a highly populated PSF, truncated by the extraction region). In the case where the parent population standard deviation is not known, a roughly 68% confidence interval for the population mean (i.e., statistical uncertainty on source position) would be $1.0 S/\sqrt{N}$, where S is the observed sample standard deviation. This is true for large N. For small samples the confidence interval becomes $t(S/\sqrt{N})$, where t is the confidence level of Student's *T*-distribution, whose exact shape depends on N (see, e.g., in Lyons 1993, p. 86). For an infinite number of N the Student's *T*-distribution is the same as the Gaussian distribution.

TABLE 3
TENTATIVE COUP SOURCES

Source	R.A. (J2000.0) (deg)	Decl. (J2000.0) (deg)
053503.8−051758	83.765885	−5.299651
053503.9−052253	83.766622	−5.381438
053504.0−052809	83.766730	−5.469410
053504.5−051908	83.768862	−5.318981
053505.7−052616	83.774150	−5.437980
053508.6−052022	83.785996	−5.339450
053508.8−052015	83.786847	−5.337515
053509.8−052143	83.791170	−5.362130
053510.4−052430	83.793640	−5.408600
053510.7−051940	83.794591	−5.327879
053512.8−052156	83.803440	−5.365780
053513.2−052322	83.805251	−5.389650
053513.5−052209	83.806492	−5.369288
053515.7−052639	83.815740	−5.444270
053528.1−051456	83.867420	−5.249130
053528.1−051958	83.867327	−5.333052

Column (8) defines the type of the source detection. The first digit indicates the image on which wavdetect found the source: 1, total band image; 2, soft band image only; 3, hard band image only; and 4, total band image with background filtered in Very Faint mode only. The great majority of sources (1522 of 1616) were found in the total band image; still, 45 sources were found only in the soft band, and 36 only in the hard band. The second digit indicates the type of event list on which a source was detected using PWDetect: 1, merged event list filtered in Very Faint mode; and 2, merged SER corrected event list.

Column (9) indicates parameters of the detection procedure. The first digit refers to wavdetect, where 1 is the probability threshold $P = 1 \times 10^{-6}$ and 2 is the probability threshold $P = 1 \times 10^{-5}$. A "1" in the second digit indicates that the source was detected with the PWDetect algorithm only. A nonzero entry in the third digit indicates that the source was found only by visual inspection. Here "1" sources were found by both the Penn State and Palermo groups, "2" sources were found only by the Penn State group, and "3" sources were found only by the Palermo group. A total of 123 of the 1616 sources were found only by visual inspection.

Column (10) gives the source significance calculated by acis_extract, which indicates how many times the source's net (background-subtracted) counts exceed the uncertainty on that quantity: SigAE = NetCts/σ(NetCts) (§ 5). Column (11) defines the probability of source existence, expressed in Gaussian sigmas calculated by PWDetect.

Columns (12) and (13) list the source counterparts from previous *Chandra* studies with the ACIS (Feigelson et al. 2002a) and HRC (Flaccomio et al. 2003a) detectors. Counterparts to earlier *Einstein*, *ROSAT*, and *ASCA* sources are given by Feigelson et al. (2002a).

Table 3 lists the 16 tentative sources that passed the Penn State and Palermo source detection criteria but did not have >3 net counts after photon extraction. Here we give only positions. These possible sources are not discussed further in this paper. The photometry results for those very weak sources strongly depend on the way local backgrounds are chosen. By introducing a manually selected local background (§ 5), we may improve their photometry and reconsider our preliminary decision on whether

these are real or tentative sources. This work will be done in a COUP membership paper, Getman et al. (2005).

5. PHOTON EXTRACTION

The acis_extract package is used to extract source photons, refine the accuracy of source positions, estimate local background, construct source and background spectra, compute redistribution matrix files (RMFs) and auxiliary response files (ARFs), construct light curves and time-energy diagrams, perform a Kolmogorov-Smirnov variability test, compute photometric properties, and perform automated spectral grouping and fitting. The reader is referred to the acis_extract Users Guide[16] for further details on the implementation of each step. The quantities derived in the photon extraction stage are listed in Table 4, and we refer to the columns of this table in this section.

Selection of an optimal extraction region for each source is not a simple task; one seeks a balance between a larger region maximizing the source's signal and (for weak sources) a smaller region minimizing the background's signal. The size and shape of the extraction region vary greatly over the field of view and cannot be parameterized accurately by an analytical expression. The acis_extract program treats these difficulties by extracting the events around the source centroid (initially, the wavdetect position) inside a polygonal contour of the local PSF, obtained with the CIAO tool mkpsf. The user need only specify the fraction of the enclosed energy desired for the extraction. For most sources, we chose to extract events from the polygonal contours of ∼87% encircled energy using PSFs at the fiducial energy of 1.497 keV. For ∼250 weak and crowded COUP sources, we chose smaller PSF contours ranging from 20% to 80% encircled energy.

While the ACIS-I instrumental background level is usually spatially invariant, it can change substantially across the COUP field due to the PSF wings and readout trails of the strong sources. We therefore adopt the procedure used in acis_extract for automatically measuring and subtracting a local background individually for each source. The background extraction region starts with a circular annulus in which the inner radius circumscribes the ∼1.1 × 97% PSF polygon and the outer radius is set such that the background region accumulated >100 events. These background events are obtained from a special background image that has excluded all events within the ∼1.1 × 97% PSF circles of all 1616 sources, so background events for one source are not corrupted by source events from neighboring sources.

The acis_extract program can also accept a user-generated background to accommodate unusual sources. The local background region was manually adjusted for 57 weak sources located in crowded fields, near or on readout trails, or on PSF wings of bright sources. Improvement of the local background is shown in Figure 4 for the sample COUP source 780. The spectrum to the left is extracted with the automatically subtracted background R_1, while the spectrum to the right is more realistic, obtained by subtracting the manually chosen background R_2. Even with such care, some faint sources may still have spectra that are corrupted by incorrect background subtraction.

Results from the photon extraction procedure appear in Table 4. The source counts tabulated in column (3) give the number of counts in the total (0.5–8 keV) energy band extracted for each source (including background). Column (4) gives the number of background counts in the total band scaled to the extracted

---

[16] Users Guide for acis_extract can be found online at http://www.astro.psu.edu/xray/docs/TARA/ae_users_guide/.

TABLE 4
COUP Source X-Ray Photometry

| | SOURCE | EXTRACTION | | | | | FLUX | | | HARDNESS | | | | | | |
Sequence Number (1)	COUP J (2)	Source Counts (3)	Background Counts (4)	NetCts (5)	Area (pixels) (6)	PSF Frac. (7)	Exp. (ks) (8)	Ct. Fl.[a] (9)	Inc. Fl.[b] (10)	MedE (keV) (11)	HR1 (12)	ΔHR1 (13)	HR2 (14)	ΔHR2 (15)	HR3 (16)	ΔHR3 (17)
1.................	053429.4−052337	883	89	793	664	0.50	500.4	0.283	−4.897	1.28	−0.59	+0.04 / −0.04	−0.54	+0.04 / −0.03	−0.34	+0.08 / −0.08
2.................	053429.5−052354	1884	53	1830	1245	0.68	157.4	0.089	−4.308	1.19	−0.69	+0.02 / −0.02	−0.67	+0.02 / −0.02	−0.28	+0.05 / −0.05
3.................	053433.9−052211	148	132	15	1541	0.89	382.0	0.216	−6.737	0.88	−1.00	+0.06 / −...	−1.00	+0.40 / −...	...	...
4.................	053434.9−052507	327	310	16	1678	0.89	527.0	0.298	−6.986	5.02	1.00	+... / −0.00	...	...	1.00	+... / −0.00
5.................	053438.2−052338	139	70	68	396	0.69	740.9	0.419	−6.292	4.69	0.75	+0.19 / −0.20	−0.22	+0.45 / −0.88	0.81	+0.17 / −0.16
6.................	053438.2−052423	2260	372	1887	994	0.90	740.9	0.419	−4.974	1.26	−0.66	+0.04 / −0.03	−0.61	+0.03 / −0.03	−0.46	+0.11 / −0.11
7.................	053439.7−052425	42315	362	41952	846	0.89	746.2	0.422	−3.630	1.20	−0.72	+0.00 / −0.00	−0.67	+0.00 / −0.00	−0.37	+0.01 / −0.01
8.................	053439.8−052456	1349	219	1129	866	0.90	746.2	0.422	−5.201	2.59	0.25	+0.04 / −0.04	0.06	+0.05 / −0.05	0.22	+0.04 / −0.04
9.................	053439.9−052642	16471	199	16271	1318	0.99	385.5	0.218	−3.757	1.34	−0.59	+0.01 / −0.01	−0.57	+0.01 / −0.01	−0.27	+0.01 / −0.01
10................	053440.0−052604	388	235	152	1118	0.88	742.7	0.420	−6.062	0.99	−0.61	+0.25 / −0.31	−1.00	+0.23 / −...	...	...
11................	053440.8−052242	5824	123	5700	691	0.88	693.2	0.392	−4.415	1.53	−0.40	+0.01 / −0.01	−0.39	+0.01 / −0.01	−0.18	+0.02 / −0.02
12................	053440.8−052639	374	42	331	228	0.39	702.0	0.397	−5.297	1.79	−0.15	+0.06 / −0.06	−0.27	+0.07 / −0.07	0.03	+0.09 / −0.09
13................	053440.9−052559	325	250	74	970	0.89	746.2	0.422	−6.380	1.11	−1.00	+0.54 / −...	−0.24	+0.24 / −0.29	−1.00	+0.89 / −...
14................	053441.6−052357	349	136	212	666	0.89	721.5	0.408	−5.908	1.00	−0.82	+0.14 / −0.14	−0.80	+0.09 / −0.08	−0.69	+0.65 / −...
15................	053441.7−052652	1758	282	1475	1103	0.88	698.5	0.395	−5.034	1.29	−0.45	+0.04 / −0.04	−0.62	+0.04 / −0.03	0.13	+0.08 / −0.08

Notes.—See § 5 for descriptions of the columns. Table 4 is available in its entirety in the electronic edition of the *Astrophysical Journal Supplement*. A portion is shown here for guidance regarding its form and content.

[a] The units for the counts-to-flux conversion factor are 10^9 counts s cm^2 photon^{-1}.

[b] The units for the log incident flux are photons cm^{-2} s^{-1}.

area corrected for small differences that may be present in the exposure maps of the source and background regions. The net or background-corrected counts appear in column (5); this is the difference between columns (3) (extracted source counts) and (4) (scaled local background counts). Columns (6) and (7) give the area of the extraction polygon in $0.''5 \times 0.''5$ pixels and the fraction of the PSF at the fiducial energy of 1.497 keV enclosed within the extracted area.

Spectral analysis requires calibration files (ARFs and RMFs) specifying the effective area and spectral resolution of the instrument at each source location as a function of energy. As the Penn State CTI corrector has been applied to the COUP event data (§ 3), there is no need to calculate RMFs for each source individually. Given the source location on each CCD chip, we select the appropriate RMF from a standard suite provided with the CTI corrector.

Source-specific ARF files are then calculated using the energy grid specified in these RMFs (685 PI channels, or 410 energy bands). In cases where a source spans multiple CCDs due to satellite dithering, the ARFs were calculated for both CCDs and summed. A further correction to the ARFs is applied to account for the energy dependence of the source PSF that falls outside the extraction region. PSFs were constructed at five fiducial energies between 0.27 and 8.6 keV (0.277, 1.497, 4.510, 6.400, and 8.600 keV), the polygonal source extraction region was applied to each PSF, the PSF fraction was computed at each available energy, and the ARF was reduced by this PSF fraction curve. The ARF was also corrected for the hydrocarbon build-up on the ACIS filters using the correction curve supplied by the tool acisabs.[17]

The "effective" exposure time at the source location is given in column (8). This quantity is derived by normalizing the ratio of an average exposure map ("Ct_Fl") to the one obtained for the region with the maximum value of the exposure map. Specifically, Exp = (CtFl/CtFl$_{max}$) × 838 ks, where 838 ks is

[17] A description of the acisabs procedure can be found online at http://www.astro.psu.edu/users/chartas/xcontdir/xcont.html.

the COUP "observed" exposure time (sum of all exposures in Table 1). This quantity summarizes the variation in the "depth" to which the sources were observed. Column (9) gives the value of the exposure map averaged over the source region (Ct_Fl) in units of 10^9 counts s cm^2 photon^{-1} and represents a conversion factor between a photon incident flux and detected counts.

The final eight columns of Table 4 provide a variety of nonparametric measures of the source flux and spectrum. Column (10) gives a rough estimate of the incident flux at the telescope aperture in units of photons cm^{-2} s^{-1}: IncFl = NetCts/⟨ARF⟩/Exp. Note that this flux estimate becomes inaccurate when the spectrum is not flat over the total 0.5–8 keV band covered by the ARF. Summing the fluxes computed over narrow energy bands will produce a more accurate result, and parametric spectral fitting (§ 7) should produce the most accurate flux estimates. Column (11) gives the background-corrected median photon energy MedE in the 0.5–8.0 keV range. IncFl and MedE can be used together for estimating the luminosities of weak sources (say, NetCts ≲ 20) for which nonlinear spectral fitting packages are ineffective (§ 9).

Columns (12)–(17) describe three hardness ratios and their 1 σ upper and lower statistical errors. The hardness ratios are defined by HR = (Cts$_h$ − Cts$_s$)/(Cts$_h$ + Cts$_s$), where subscripts "h" and "s" refer to a harder and softer band, respectively. For COUP, we define HR1 to reproduce the commonly used hardness ratio between the $s = 0.5$–2.0 keV and $h = 2.0$–8.0 keV bands, HR2 to highlight the softer part of the spectrum between $s = 0.5$–1.7 keV and $h = 1.7$–2.8 keV, and HR3 to measure the harder part of the spectrum between $s = 1.7$–2.8 keV and $h = 2.8$–8.0 keV. For each energy band, acis_extract computes the net counts corrected for the local background in the appropriate band. Confidence intervals encompassing 68% of the expected error, equivalent to ±1 σ in a Gaussian distribution, are estimated first by calculating upper and lower errors on total and background counts using Gehrels (1986, eqs. [7] and [12]) and then propagating those errors to net counts using Lyons (1993, eq. [1.31]). We then propagate errors from net counts to upper and lower uncertainties on hardness ratios using the method
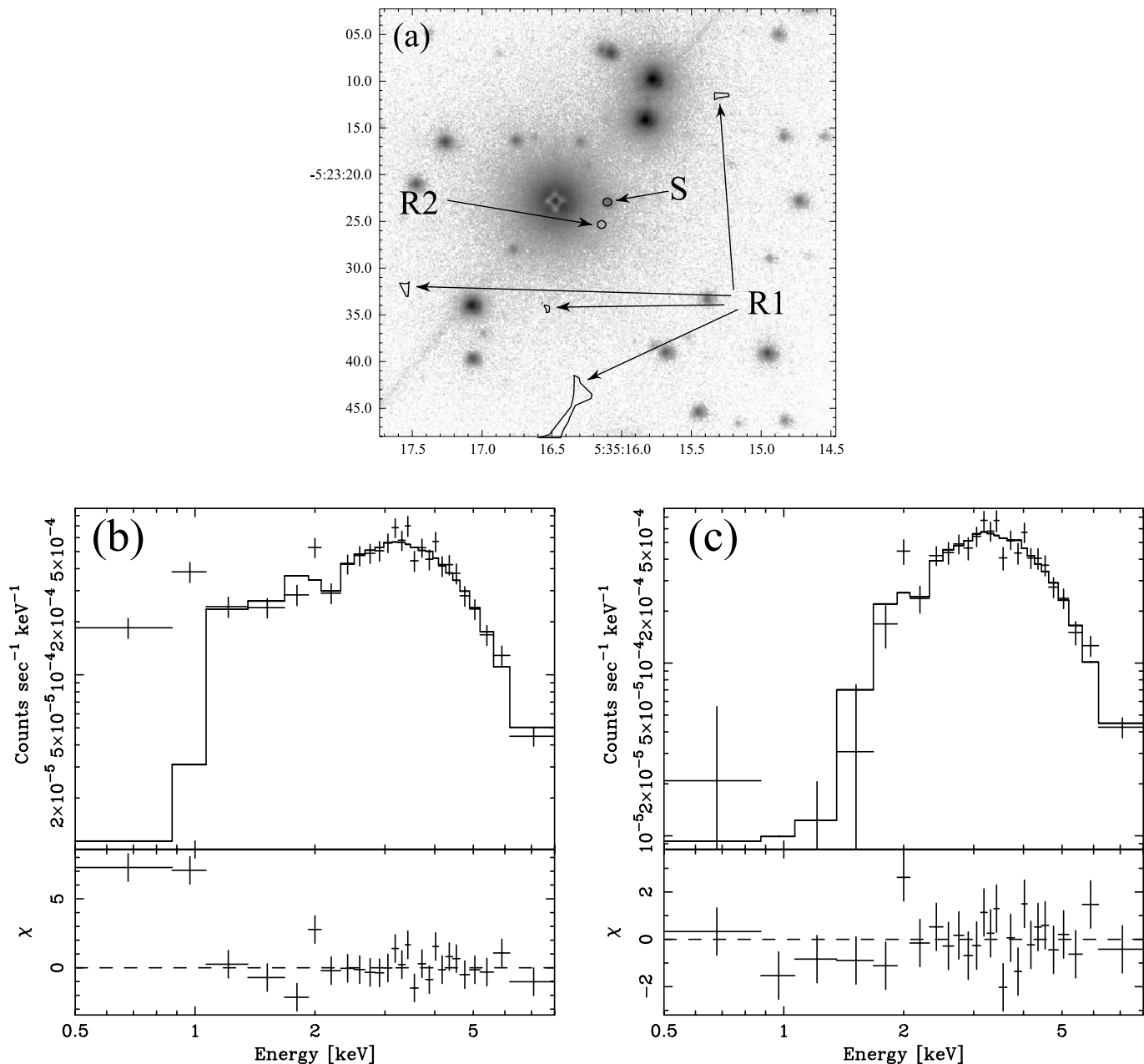
Fig. 4.—(a) Close-up view of the neighborhood of the sample source COUP 780, located in a region of highly nonuniform background. "R1" marks the automatically extracted background region, "R2" is the manually improved local background, and "S" indicates the source extraction region. Bottom panels show spectra obtained through the subtraction of the automatically extracted background (b), and improved manually chosen background (c).

in Lyons (1993). When net counts are negative in an energy band we clip them at zero (to ensure that hardness ratios are bounded by $[-1, 1]$) and choose to set their lower errors to zero. In cases where the 68% confidence interval of soft band net counts contains zero (very hard sources), we consider the upper uncertainties on hardness ratios to be unreliable and do not report them; similarly, we do not report the lower uncertainties on hardness ratios of very soft sources. When the 68% confidence interval of both bands contains zero counts we do not report hardness ratios, because their errors would be large.

6. STRONG SOURCES WITH PHOTON PILE-UP

A few dozen COUP X-ray sources are simultaneously sufficiently strong and close to the aim point with narrow PSFs to suffer photon pile-up. This occurs when two or more photons are incident on a single CCD pixel during a single 3.2 s CCD frame. Some of these pile-up events mimic cosmic rays and are rejected by the on-board computer, while others are telemetered as valid events but with spuriously high energies. While statistical reconstruction treatments of ACIS pile-up have been developed (Davis 2001; Kang et al. 2003), the approach adopted here is to discard events at the core of the PSF, which are both spatially and spectrally distorted, and to use only ordinary, pile-up–free events in the outskirts of the PSF (Broos et al. 1998).

Our procedure is to extract events from circular annuli between radii r_{in} and r_{out} (the latter was usually fixed around the 99% enclosed energy contour) and to construct specialized ARFs associated with those annuli at the particular source location.
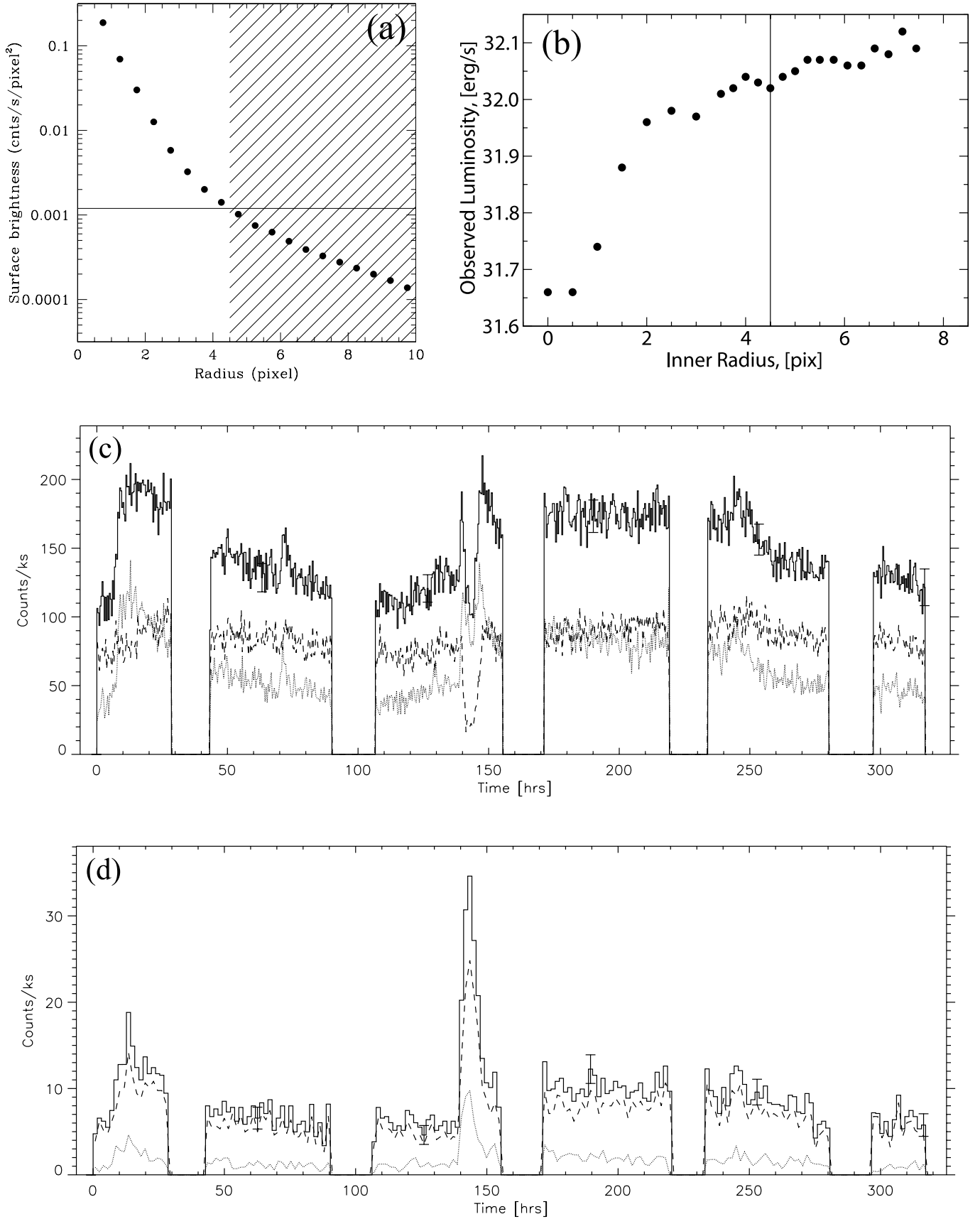
FIG. 5.—Study of the heavily piled-up COUP source 932: (*a*) the radial surface brightness profile of the piled-up events; (*b*) the inferred source luminosity as a function r_{in} in our annular extraction technique for a series of excluded core sizes (solid line marks the ~2% pile-up fraction); (*c*) light curve extracted from the usual extraction region including pile-up; and (*d*) light curve from the optimal annular extraction region. In the light curves, the solid line indicates the total energy band (0.5–8 keV), the dashed line indicates the soft band (0.5–2.0 keV), and the dotted line indicates the hard band (2.0–8.0 keV). Note that (*c*) shows a spurious dip, while (*d*) shows the correct flare.

TABLE 5
COUP SOURCES WITH PILE-UP ANALYSIS

Sequence Number	COUP J	r_{in} (0″5 pixel)	r_{out} (0″5 pixel)	NetCts	PSF Fraction
107	053455.9−052313	6.25	12.67	9004	0.08
123	053457.7−052351	5.00	11.95	5347	0.10
124	053457.7−052352	4.50	11.96	5074	0.13
245	053505.6−052519	3.50	11.73	2426	0.05
290	053507.4−052640	1.50	9.94	1895	0.51
394	053510.7−052344	2.50	9.14	4051	0.04
430	053511.5−052602	3.00	10.05	3621	0.06
450	053511.8−052149	4.00	9.95	5327	0.02
689	053515.2−052256	2.50	8.59	6931	0.03
724	053515.6−052256	4.00	8.54	3504	0.01
732	053515.7−052309	2.25	8.44	37523	0.04
745	053515.8−052314	2.25	8.39	21283	0.02
809[a]	053516.4−052322	5.25	8.43	63444	0.01
854	053517.0−052232	2.25	8.64	3829	0.05
855	053517.0−052334	3.00	8.75	3364	0.02
881	053517.3−052544	3.75	9.73	4521	0.02
891	053517.5−051740	6.00	16.56	12686	0.17
932	053517.9−052245	4.50	8.45	6648	0.01
965	053518.3−052237	3.50	8.56	5939	0.02
1087	053520.1−052639	4.00	10.81	3792	0.02
1090	053520.2−052056	3.00	10.31	4306	0.05
1130	053521.0−052349	3.00	8.99	3843	0.03
1232	053522.8−052457	4.25	9.66	3525	0.01
1259	053523.6−052331	2.50	9.40	2183	0.04

[a] θ^1C Ori.

The ARF correction is made using the xpsf tool developed by G. Chartas,[18] which uses MARX simulated sources to establish the energy-dependent fraction of photons in the extracted annulus. The challenge is to find the smallest r_{in} that gives the greatest number of counts available for later analysis without reducing the inferred source flux because of photon pile-up. The best r_{in} was established for each source by repeated trials.[19] We found that the best r_{in} typically occurs at a surface brightness of $\sim 1.2 \times 10^{-3}$ counts s^{-1} pixel^{-1}, which roughly corresponds to a pile-up fraction of $\sim 2\%$, or when the flux profile reaches a plateau. This is seen in the top two panels of Figure 5 for the heavily piled-up COUP source 932. Figure 5a presents the brightness profile

[18] Description of the procedure based on the algorithm of xpsf.pro can be found online at http://www.astro.psu.edu/users/tsujimot/arfcorr.html.

[19] More information can be found at http://www.astro.psu.edu/xray/docs/TARA/ae_users_guide/pileup.txt.

TABLE 6
COUP SOURCE X-RAY SPECTROSCOPY

Sequence Number (1)	COUP J (2)	log N_H (cm^{-2}) (3)	Δ log N_H (cm^{-2}) (4)	kT_1 (keV) (5)	ΔkT_1 (keV) (6)	kT_2 (keV) (7)	ΔkT_2 (keV) (8)	log EM$_1$ (cm^{-3}) (9)	σ (cm^{-3}) (10)	log EM$_2$ (cm^{-3}) (11)	σ (cm^{-3}) (12)	χ^2_ν (13)	dof Flag (14)	Fit Flag (15)	Model Flag (16)	Feature (17)
1	053429.4−052337	20.67	0.43	0.85	0.12	4.37	0.95	52.17	0.11	52.62	0.04	1.15	33	…	20.1.2	000c0000
2	053429.5−052354	21.21	0.07	0.79	0.03	3.29	0.35	53.13	0.06	53.16	0.04	1.15	23	…	60.1.2	00000000
3	053433.9−052211	20.21	2.31	1.14	0.27	…	…	51.28	0.25	…		0.70	24	…	05.1.1	00h00000
4	053434.9−052507	23.39	0.27	1.44	4.39	…	…	53.72	1.00	…		0.65	58	…	05.1.1g	0s000000
5	053438.2−052338	23.46	0.21	9.52	15.00	…	…	52.61	0.44	…		1.15	24	…	05.1.1	0s000m00
6	053438.2−052423	21.12	0.12	0.78	0.09	2.32	0.27	52.16	0.12	52.68	0.04	1.15	28	…	60.1.2	000c0000
7	053439.7−052425	20.93	0.04	0.83	0.01	2.30	0.08	53.58	0.02	53.94	0.01	2.06	173	m	60.1.2	100000w0
8	053439.8−052456	22.05	0.05	15.00	8.48	…	…	52.81	0.02	…		0.95	18	…	60.1.1	00000000
9	053439.9−052642	21.37	0.03	0.83	0.02	3.04	0.11	53.59	0.03	53.87	0.01	1.38	134	p	60.1.2g	00000000
10	053440.0−052604	20.00	1.21	0.74	0.13	…	…	51.42	0.21	…		0.77	44	…	07.1.1	00h00000
11	053440.8−052242	21.69	0.04	0.52	0.03	4.13	0.29	53.21	0.12	53.34	0.02	1.81	70	p	60.1.2	l0000000
12	053440.8−052639	21.33	0.18	14.34	11.68	…	…	52.44	0.05	…		0.68	32	…	10.1.1	00000000
13	053440.9−052559	20.00	2.12	12.58	15.00	…	…	51.51	0.17	…		1.02	55	…	05.1.1	00h00p00
14	053441.6−052357	20.81	0.14	0.69	6.24	9.23	15.00	51.64	1.00	51.19	0.21	0.75	25	…	10.1.2	00hc0000
15	053441.7−052652	21.16	0.44	0.66	0.08	15.00	15.00	52.35	0.16	52.59	0.03	1.60	21	m	60.1.2	00h00000

NOTES.—See § 7 for descriptions of the columns. Table 6 is available in its entirety in the electronic edition of the *Astrophysical Journal Supplement*. A portion is shown here for guidance regarding its form and content.

with the dashed line marking the level of $\sim$2% pile-up fraction, and Figure 5*b* presents the luminosity (flux $\times 4\pi D^2$) profile obtained from the spectral fits of consequently diminishing annuli.

Sixty-five strong and centrally concentrated COUP sources were examined in this fashion; these sources are flagged with a "p" in Table 2. Only 24 sources were found to require the annular extraction analysis, with results given in Table 5. Those 24 piled-up sources are also flagged with an "a" in Table 6 (see § 7 below). All further analysis for them (photometry, spectroscopy, and variability) was performed with the annular extracted events. It is particularly critical that variability not be studied using the central piled-up core of these sources: flares often saturate and can even appear as plateaus or sudden dips in the count rates. An example of this spurious result is shown in Figures 5*c* and 5*d*, where Figure 5*c* presents the light curve extracted from the usual extraction region including pile-up, while Figure 5*d* shows the light curve from the optimal annular extraction region.

7. SPECTRAL ANALYSIS

A goal of the present study is to produce an *acceptable* spectral model for the 1616 sources to give reliable time-averaged broadband luminosities and preliminary characterization of intrinsic spectral properties and interstellar absorption. We recognize that the semiautomated approach here using the `acis_extract` package will often not produce the *best* spectral model. Other COUP studies will analyze selected sources in much more detail, studying interstellar absorptions, plasma elemental abundances, time-variations of temperatures, and so forth. We describe the `acis_extract` spectral analysis procedure here.

For each of the 1616 COUP sources, the CIAO tool `dmextract` is first called to create a HEASARC/OGIP-compatible type I source spectrum over the energy range 0–10 keV, or PI channel range 0–685 compatible with the Penn State CTI-corrected RMFs. The BACKSCAL keywords in the source and background spectra are the integral of the exposure map over the source and background regions. An algorithm for grouping spectra was implemented using custom code inside `acis_extract`, rather than via the grouping tools in FTOOLS (`grppha`) or CIAO (`dmgroup`), in order to place the first and last grouping bin boundaries at specified energies so that the spectra examined always have the range 0.5–8.0 keV. These boundaries are controlled by specifying PI = 1–34 (energy <0.5 keV) for the first group and PI = 549–685 (energy ≥8.0 keV) for the last group. For the intermediate channels PI = 35–548 of scientific interest, channels were grouped according to the following scheme: each group contains at least 5 events for sources with NetCts < 100, at least 7 events for $100 \leq$ NetCts < 200, at least 10 events for $200 \leq$ NetCts < 500, at least 20 events for $500 \leq$ NetCts < 1000, and at least 60 events for NetCts ≥ 1000. Simulations show that biases to the inferred temperatures when $kT \geq 10$ keV and to the column densities when $\log N_{\rm H} \leq 20.5$ cm^{-2} may be present when groups have NetCts ≤ 10 events (Feigelson et al. 2002a, § 2.8).

Automated spectral fitting is performed by `acis_extract` by spawning the XSPEC spectral fitting program (Arnaud 1996). In most cases, spectra fits were found with one- and two-temperature optically thin thermal plasma MEKAL models (Mewe 1991), assuming a uniform density plasma with 0.3 times solar elemental abundances (Imanishi et al. 2001; Feigelson et al. 2002a). While these fits are usually statistically successful, the assumptions are clearly astrophysically inadequate. Detailed studies of magnetically active stars show that many plasma components with a wide range of temperatures may be present and that chemical

fractionation associated with magnetic reconnection flaring can produce strongly nonsolar elemental abundance distributions (e.g., Kastner et al. 2002; Audard et al. 2003). X-ray absorption was modeled using the atomic cross sections of Morrison & McCammon (1983) with traditional solar abundances to infer a total (mainly hydrogen and helium) interstellar column density, $\log N_{\rm H}$, in units of (atoms cm^{-2}).[20] Here again, the astrophysical situation may be more complex with untraditional elemental abundances or gas-to-dust ratios (Vuong et al. 2003).

Acceptable spectral fits were obtained by minimizing χ^2 between the grouped ACIS spectra and the parametric plasma models. We starting the fitting process in two ways: fixed standard values of the model parameters ($\log N_{\rm H} = 21.3$ cm^{-2}, $kT_1 = 1.0$, and $kT_2 = 3.0$ keV), and a grid of initial parameters. The final result was chosen by visual inspection using the `acis_extract` accessory tool `spectra_viewer`, based on three criteria. First, for sources with NetCts $\lesssim 200$, one-temperature plasma models were used if they fit. Second, for hard sources with median energy MedE $\gtrsim 2$ keV, a one-temperature model fit was again chosen to avoid the highly nonlinear interaction of an unseen soft component and uncertain interstellar absorption. Third, for the brighter and softer sources (MedE $\lesssim 2$ keV, NetCts $\gtrsim 200$), two-temperature plasma fits were typically needed to obtain good fits. Uncertainties to each spectral parameter are estimated by a $\Delta\chi^2_{\rm min} +$ constant criterion using the `error` command in XSPEC.

Emission measures were calculated using the best-fit normalizations from XSPEC as EM $= 10^{14} \times$ norm $\times 4\pi D^2$. In cases of two-temperature fits, both emission measures for soft and hard components are provided.

We emphasize again that the resulting spectral parameters and their uncertainties are often not reliably determined and that alternative models may be similarly successful. The greatest uncertainty in plasma temperatures and emission measures occurs for sources with high absorption, $\log N_{\rm H} \simeq 22-23$ cm^{-2}. Here we have no direct knowledge of the soft emission that, in less absorbed sources, typically dominates the hard emission. Thus, our approach here may severely underestimate broadband 0.5–8 keV luminosities of heavily absorbed sources, although luminosities in the hard 2–8 keV band are more reliable.

A second common source of uncertainty occurs for strong COUP sources where two qualitatively different spectral models give similarly good values of χ^2. Figure 6 shows a typical example; the left panel shows the solution with the lower energy kT_1 of 0.1–0.3 keV and higher energy kT_2 of 1–2 keV, while the right panel presents another solution with $kT_1 \sim 0.6-0.9$ keV, $kT_2 \sim 2-3$ keV. Such ambiguities in spectral parameters occur in $\sim$150 bright COUP sources. We have chosen here to present the second class of solution that avoids the inference of a very luminous, heavily absorbed, ultrasoft ($kT_1 < 0.5$ keV) component. The errors in XSPEC parameters do not take into account the possibility that we have chosen the incorrect acceptable model.

The results of our spectral analysis are tabulated in Table 6. One-temperature spectral fit results are recorded for 980 COUP sources and two-temperature results for 563 sources. Spectral models for 73 sources with very poor statistics (NetCts < 20)

---

[20] Three strong COUP X-ray sources with complex spectra required two absorption components to achieve an acceptable spectral fit (in XSPEC, this model is specified wabs $\times$ mekal + wabs $\times$ mekal). These column densities were, for the three sources, respectively, $\log N_{\rm H1} < 20$ and $\log N_{\rm H2} = 22.3$ for COUP source 267; $\log N_{\rm H1} = 21.6$ and $\log N_{\rm H2} = 22.8$ for 578; and $\log N_{\rm H1} \sim 20.9$ and $\log N_{\rm H2} \sim 22.8$ for 948. These values are not reported in Table 6. It is not clear whether the two components are astrophysically real (e.g., an unresolved double source with different absorptions) or result from poor spectral model specification.
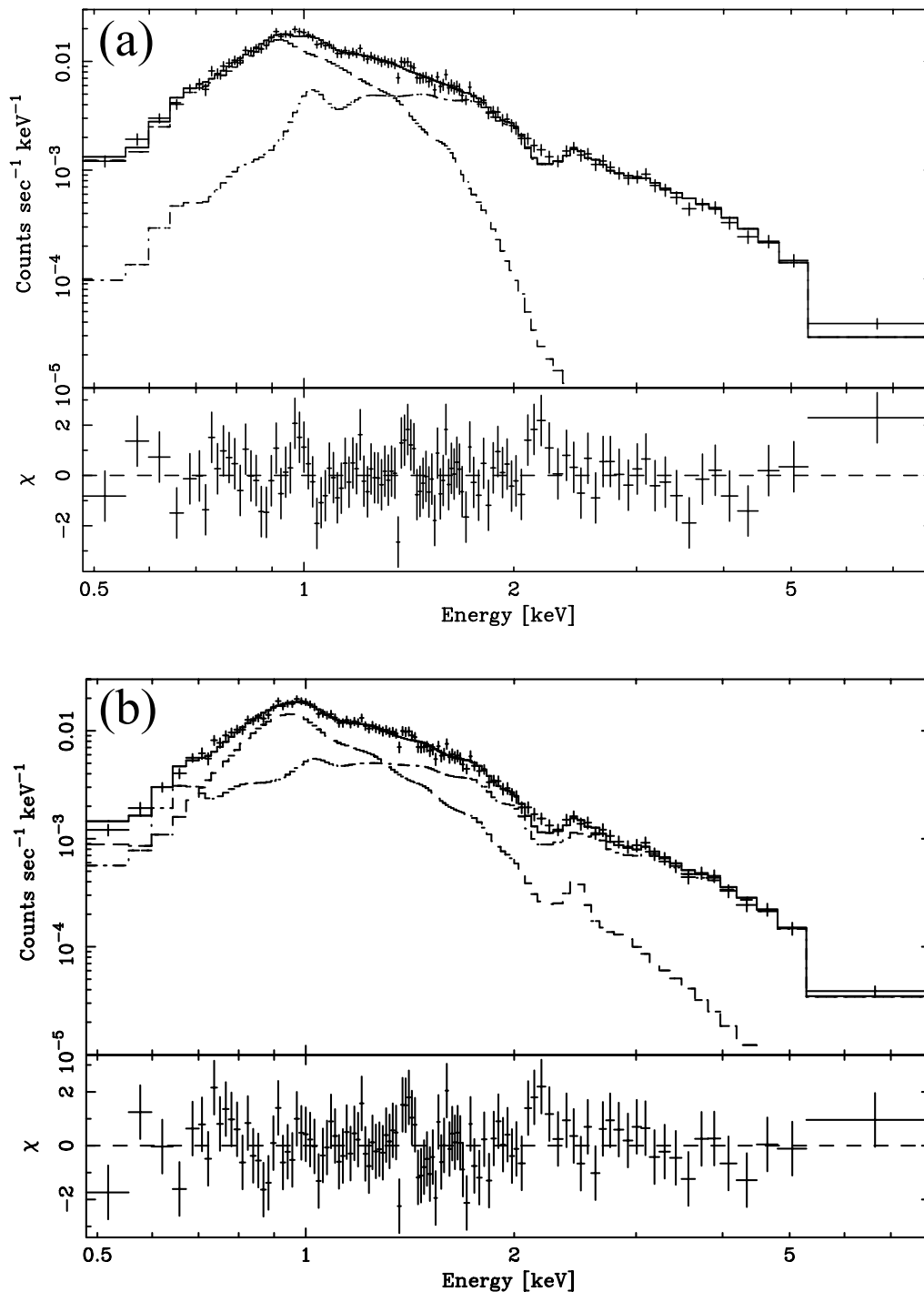
Fig. 6.—Spectrum of COUP source 567 exemplifying a common ambiguity in spectral fitting. Panel (*a*) presents a fit with $kT_1 \approx 0.2$ keV, $kT_2 \approx 1.7$ keV, $\log N_H \approx 21.8$ cm^{-2}, and $\log L_{t,c} \approx 31.6$ ergs s^{-1} with a reduced $\chi^2 \approx 1.3$. Panel (*b*) presents another fit (which appears in Table 6) with $kT_1 \approx 0.8$ keV, $kT_2 \approx 3.1$ keV, $\log N_H \approx 21.3$ cm^{-2}, $\log L_{t,c} \approx 30.6$ ergs s^{-1}, and a reduced $\chi^2 \approx 1.4$. Note the tenfold difference in inferred unabsorbed luminosity in the total 0.5–8 keV band.

are left blank. Columns (3) and (4) report the logarithm of the hydrogen column density and its 1 σ error in cm^{-2}, obtained from the spectral fit. Fitted values with $\log N_H < 20.0$ cm^{-2} are truncated at 20.0 because ACIS-I spectra are insensitive to differences in very low column densities. Columns (5) and (6) give the plasma energy and its 1 σ error in keV; in cases of two-temperature fits, this is the energy of the soft component. Columns (7) and (8) give the plasma energy of the hard component and its 1 σ error in two-temperature model fits. Fitted values with $kT > 15$ keV are truncated at 15 keV because the

data cannot discriminate between very high-temperature values. Columns (9)–(12) report the emission measures and their 1 σ errors in the units of cm^{-3} for each temperature component. Columns (13) and (14) give the reduced χ^2_ν for the overall spectral fit and degrees of freedom, respectively.

Details regarding the spectral fitting process for individual sources are provided by the flags in columns (15)–(16). Column (15) marks sources where the model was formally inadequate, based on the null hypothesis probability P_χ of χ^2 for the relevant degrees of freedom: "m" indicates a marginal fit

TABLE 7
COUP Source X-Ray Variability

Sequence Number (1)	COUP J (2)	Gap Flag (3)	log P_{KS} (4)	BBNum (5)	BBMin. (counts ks^{-1}) (6)	ΔBBMin. (counts ks^{-1}) (7)	BBMax. (counts ks^{-1}) (8)	ΔBBMax. (counts ks^{-1}) (9)
1........................	053429.4−052337	...	−4.00	7	0.50	0.02	36.67	1.52
2........................	053429.5−052354	...	−3.40	9	1.18	0.10	64.52	14.96
3........................	053433.9−052211	...	−0.95	1	0.18	0.01	0.18	0.01
4........................	053434.9−052507	...	−0.68	1	0.39	0.01	0.39	0.01
5........................	053438.2−052338	...	−0.19	1	0.34	0.01	0.34	0.01
6........................	053438.2−052423	...	−4.00	8	0.91	0.09	10.51	0.26
7........................	053439.7−052425	...	−4.00	36	26.65	2.60	301.08	55.54
8........................	053439.8−052456	...	−1.06	1	1.61	0.02	1.61	0.02
9........................	053439.9−052642	...	−4.00	105	6.34	1.47	518.43	45.68
10......................	053440.0−052604	...	−3.00	6	0.33	0.02	21.46	2.20
11......................	053440.8−052242	...	−4.00	19	3.33	0.90	98.11	2.35
12......................	053440.8−052639	...	−4.00	5	0.29	0.02	2.08	0.16
13......................	053440.9−052559	...	−1.01	1	0.39	0.01	0.39	0.01
14......................	053441.6−052357	...	−2.70	2	0.38	0.01	1.20	0.11
15......................	053441.7−052652	...	−4.00	8	0.77	0.23	3.56	0.23

NOTES.—See § 8 for descriptions of the columns. Table 7 is available in its entirety in the electronic edition of the *Astrophysical Journal Supplement*. A portion is shown here for guidance regarding its form and content.

with $0.005 \leq P_\chi < 0.05$, and "p" indicates a poor fit with $P_\chi < 0.005$. Column (16) presents a three-part flag giving details of the spectral modeling for each source. The first part gives the minimum number of events in each spectral group. The second part indicates whether two absorption components are needed (see footnote 8). The third part gives the number of plasma components used in the accepted fit, 1 or 2. A "g" indicates that the spectral result has been chosen from a grid of initial parameter values.

Column (17) is a conjunction of eight flags giving important information on source-specific spectral features and problems, some obtained from visual inspection of the spectral fit and the location of the source in the ACIS image. The first flag (1) indicates the presence of narrow spectral features in the data that are not present in the model, probably due to elemental abundances inconsistent with our assumption of 0.3 times solar values. A total of 186 COUP sources are flagged with spectral features. Flags 2 and 3 indicate that soft (s) or hard (h) excesses were present in the data that were not in the model. In most cases, this can be attributed to poor subtraction of nonuniform local background around weak sources. The fourth flag (c) signals that the spectrum may be corrupted by a close star component. The fifth flag (p) indicates that the spectral fit is unreliable due to poor statistics and/or a poor fit based on visual examination rather than χ^2 values. The sixth flag (m) marks cases where we defined the background extraction region with a manual (rather than automatic) procedure (§ 5). The seventh flag (a) marks the 24 heavily piled-up sources requiring annular extraction, as discussed in § 6. The eighth flag (w) notes 26 additional sources that appeared weakly piled up for which the usual whole polygonal extraction region was used.

8. VARIABILITY ANALYSIS

The temporal behaviors of COUP sources are often very complex with high-amplitude, rapidly changing flares superposed on quiescent or slowly variable emission. Relegating detailed study of these behaviors to later studies, we provide here two broadly applicable measures of variability and report results in Table 7. All variability measures are made on the extracted SrcCts events without background subtraction. While the background is usually negligible and is not itself highly variable, it may play a role in the variability characteristics of off-axis weaker sources. In 33 cases when sources were located on an ACIS CCD chip gap (flagged in col. [3] of Table 7), tests have been performed on data extracted from the primary CCD only. These sources may exhibit spurious short-term variability. We are confident that the intrinsic variability of piled-up sources is accurately reflected by our annular extraction procedure (§ 6) though with reduced signal.

First, the `acis_extract` package applies the nonparametric one-sample Kolmogorov-Smirnov (K-S) test to establish whether variations are present above those expected from Poisson noise associated with a constant source. Here the cumulative distribution of photon arrival times is compared to a simple model for a constant source subject to the same gaps in observation times due to orbit perigees (Fig. 7*a*). In Table 7, column (4) reports the logarithm of test significance: probability values $\log P_{KS} \leq -3.0$ can be considered almost definitely variable, while variability has not been reliably detected when $\log P_{KS} > -2.0$. Log P_{KS} has been truncated at -4.0 for strong sources with high-amplitude variability because the tail of the statistic distribution is not well defined.

Second, we employed the Bayesian block (BB) parametric model of source variability developed by Scargle (1998). Here the light curve is segmented into a contiguous sequence of constant count rates (Fig. 7*b*). The change points between constant count rates are determined by an iterative maximum-likelihood procedure for a Poissonian process. We modeled the ACIS frame mode data stream as binned data, with modifications to cancel the COUP bad time intervals. The maximum-likelihood procedure corresponding to binned data was implemented in the IDL language.[21] BB constant count rates and boundaries were corrected for CCD readout dead times and COUP bad time intervals, respectively. The prior ratio parameter indicates the subjective preference we have for the single-rate Poisson model over the dual-rate model prior to analyzing the data. This quantity is practically useful for suppressing spurious segments due to the

---

[21] Description of this procedure and code can be found online at http://www.astro.psu.edu/users/gkosta/COUP/BBCODE/.
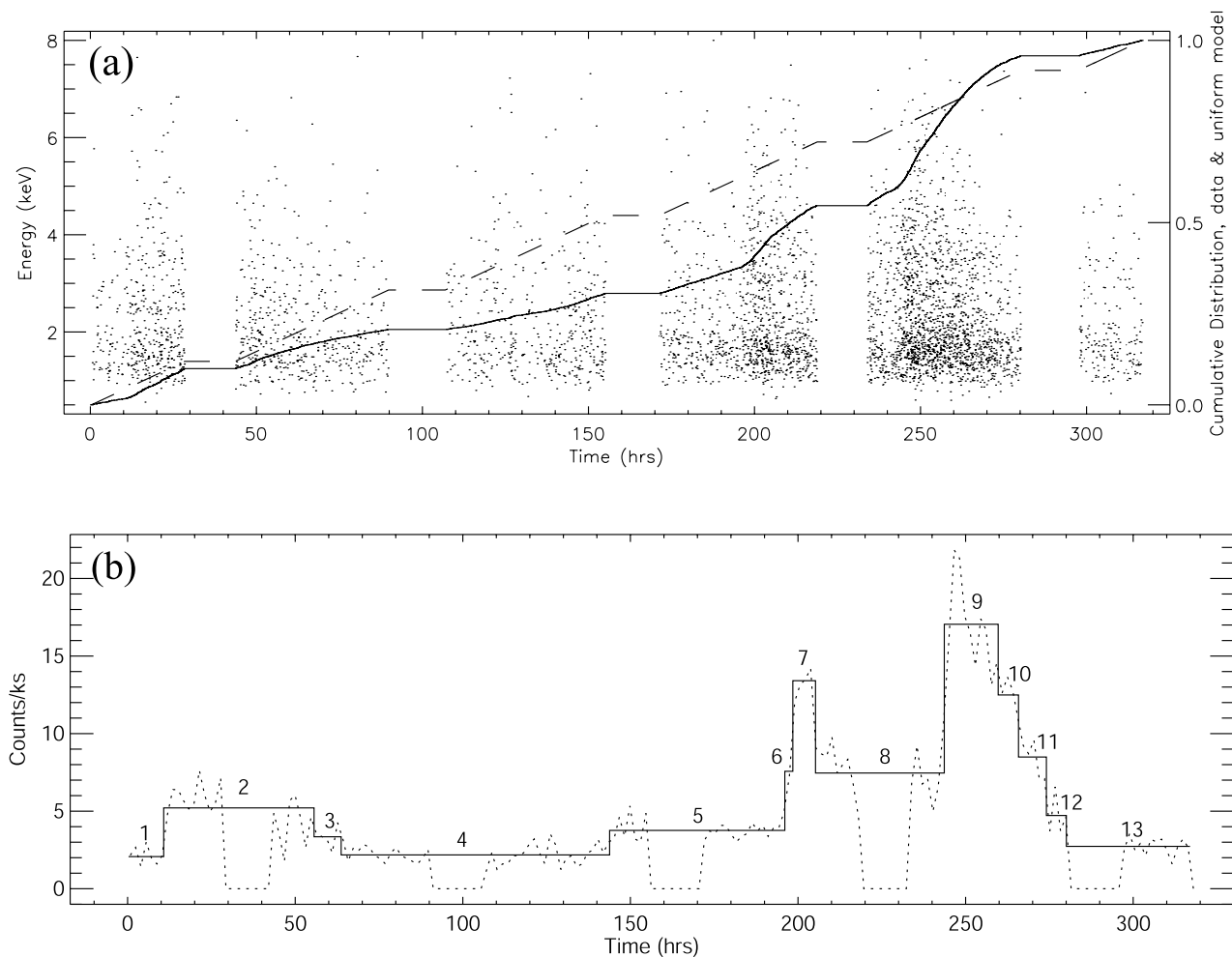
Fig. 7.—Variability analysis of COUP source 645. (*a*) Arrival times as a function of energy in the total (0.5–8.0 keV) energy band. The overplotted lines represent the cumulative distributions of the data (*solid line*) and uniform model (*dashed line*) used to compute the K-S variability test. (*b*) Bayesian blocks segmentation (*solid line*) of the X-ray light curve (*dotted line*) in the total energy band.

statistical fluctuations. We found that the overall shape of the BB light curves is insensitive to large changes in the prior ratio, from 1 up to the ratio of the length of data interval to the desired time resolution for bright COUP sources (~100–200), that is the condition to stop oversegmenting (Scargle 1998). Thus, the prior ratio parameter was assigned the unbiased value of 1.

A more important parameter is the minimum number of counts allowed in a segment, which stops the segmenting process; in many cases, the number of segments varies with this value. After experimentation, we chose a minimum of 5 counts per segment in order to achieve maximal consistency between the BB and K-S tests for marginally variable sources. Specifically, if we define a source to be BB variable if the number of segments BBNum ≥ 2 and a source to be K-S variable if $\log P_{KS} < -2.0$, then 1515 of 1616 COUP sources are consistently classified as variable or nonvariable by the two methods. With these criteria for variability, 60% (974 for K-S or 973 for BB) of the 1616 COUP sources are variable. One consequence of combining the unbiased prior ratio parameter with only 5 minimum counts per segment is that strong sources often trigger isolated short segments with a small count number. These spurious peaks are easily identified by visual examination of the BB light curve.

Columns (5)–(9) of Table 7 report the results of the BB variability analysis. They give the number of segments BBNum, the count rates of the lowest and highest segments, and their 1 σ

uncertainties (from Gehrels 1986) assuming Poisson statistics within the segment. The minimum count rate might sometimes be viewed as the quiescent level between flaring events. The ratio of maximum to minimum count rates may, within errors, be viewed as a measure of variability amplitude. We caution, however, that visual examination and individual analysis of light curves is needed for a full understanding of COUP source variability.

9. LUMINOSITIES

X-ray luminosities are provided here in three broad bands: L_s in the soft 0.5–2.0 keV band, L_h in the hard 2.0–8.0 keV band, and L_t in the total 0.5–8.0 keV band. Luminosities are calculated from fluxes F in these bands according to $L = 4\pi D^2 F$ assuming a distance $D = 450$ pc to the Orion Nebula region. For 1543 of the 1616 COUP sources, fluxes are obtained from the thermal plasma spectral fits (§ 7) using XSPEC's flux tool, which integrates the model spectrum over the desired band. Since the ARFs used with XSPEC incorporate instrumental effects, such as the unextracted PSF fraction and absorption by hydrocarbon contamination on the detector, no additional correction factors are needed at this stage. Running XSPEC's flux tool with the fitted plasma energies and emission measures but with zero absorption gives estimates of the intrinsic source emission prior to interstellar absorption. We call these absorption-"corrected" luminosities $L_{s,c}$, $L_{h,c}$, and $L_{t,c}$. Formal $\sqrt{N}$ statistical uncertainties on the
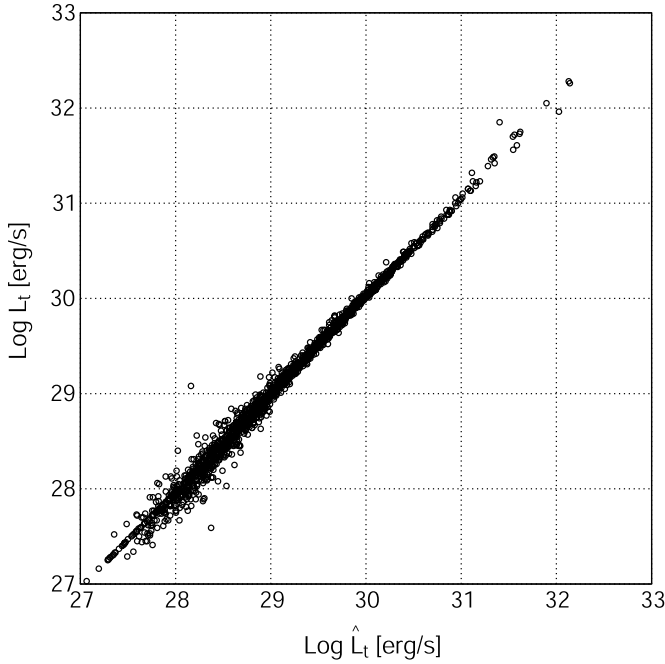
Fig. 8.—Scatter plot of total band luminosities L_t inferred from XSPEC spectral fitting with the approximate luminosity $\hat{L}_t$ derived from photometric data.

luminosity can be readily obtained from NetCts and HR1 values in Table 4. For most sources, these statistical uncertainties to the luminosities are only about ± 0.1 or less in $\log L$.

The scientific reliability of these luminosities, however, is usually considerably lower than the formal statistical uncertainty for several reasons. First, 60% of the sources exhibit temporal variability, often by factors of $0.3-1.3$ in $\log L_t$ (§ 8). Second, the measured value of L_s is often only a small fraction of the emitted soft luminosity due to interstellar absorption. There are >300 sources with fitted $\log N_H \geq 22.5$ cm^{-2}; for such heavily absorbed sources, the soft plasma component and L_s is essentially unknown from spectral fits. The average lightly

absorbed source has $L_s \simeq 2L_h$, so that the majority of the luminosity is probably missed in the heavily absorbed sources. The absorption-corrected value $\log L_{s,c}$ is so uncertain that we do not provide it for scientific analysis.

For the 73 faintest sources without any XSPEC spectral fit, we estimate the total band luminosities $\hat{L}_t \propto \mathrm{IncFl} \times \mathrm{MedE}$, where the incident flux IncFl and source's median energy MedE are given in Table 4. The basis for this approximation is the strong correlation between the $\log L_t$ values derived from the XSPEC spectral fits with the approximate $\hat{L}_t$ values shown in Figure 8. These values generally differ from each other by no more than 0.2 in $\log L$.

Columns (3)–(7) of Table 8 list $\log L_s$, $\log L_h$, $\log L_{h,c}$, $\log L_t$, and $\log L_{t,c}$.

10. STELLAR COUNTERPARTS

COUP source positions were compared with source positions from two optical catalogs, two near-infrared (JHK_s bands) catalogs, and two thermal-infrared (L band) catalogs. These catalogs differ in sensitivity and fields of view. In the optical band, we use the catalog of Hillenbrand (1997, hereafter H97) and additional stars found by Herbst et al. (2002, hereafter H02). Both of these surveys cover the full COUP field. In the JHK_s bands, we use a merged catalog developed by M. J. McCaughrean et al. (2005, in preparation, hereafter McC05) for the inner, most sensitive quarter of the COUP field and the Two Micron All-Sky Survey (2MASS; Cutri et al. 2003) for the outer portions of the field. Many of the 2MASS nondetections (i.e., 2MASS sources not detected in the COUP image) can be attributed to spurious sources in the 2MASS catalog, which lie along bright emission-line filaments of the nebula (such as the Orion Bar). In the L-band, we use the catalog of Lada et al. (2004) for a small inner region and the catalog of Muench et al. (2002, hereafter MLLA) for additional coverage around the center of the COUP field.

The JHK_s catalog provided by McC05 is particularly valuable for studies in the inner $7' \times 7'$ of the COUP field. It starts with a deep imaging survey of the inner Trapezium Cluster made using the ISAAC near-infrared camera on UT1 of the ESO Very

TABLE 8
COUP Source X-Ray Luminosities

Sequence Number (1)	COUP J (2)	$\log L_s$ (ergs s^{-1}) (3)	$\log L_h$ (ergs s^{-1}) (4)	$\log L_{h,c}$ (ergs s^{-1}) (5)	$\log L_t$ (ergs s^{-1}) (6)	$\log L_{t,c}$ (ergs s^{-1}) (7)
1	053429.4−052337	29.51	29.50	29.50	29.81	29.84
2	053429.5−052354	30.11	29.95	29.96	30.34	30.47
3	053433.9−052211	28.12	27.42	27.42	28.20	28.22
4	053434.9−052507	<27.00	29.09	30.04	29.09	30.65
5	053438.2−052338	<27.00	29.05	29.62	29.05	29.80
6	053438.2−052423	29.47	29.31	29.32	29.69	29.79
7	053439.7−052425	30.82	30.57	30.57	31.01	31.08
8	053439.8−052456	28.86	29.81	29.85	29.85	30.01
9	053439.9−052642	30.64	30.62	30.64	30.93	31.08
10	053440.0−052604	28.37	27.11	27.11	28.39	28.39
11	053440.8−052242	29.92	30.17	30.20	30.36	30.63
12	053440.8−052639	28.95	29.47	29.48	29.58	29.64
13	053440.9−052559	28.22	28.54	28.54	28.71	28.71
14	053441.6−052357	28.60	28.25	28.25	28.76	28.82
15	053441.7−052652	29.35	29.58	29.59	29.78	29.86

Notes.—See § 9 for descriptions of the columns. Table 8 is available in its entirety in the electronic edition of the *Astrophysical Journal Supplement*. A portion is shown here for guidance regarding its form and content.

TABLE 9
PROBABLE OPTICAL COUNTERPARTS OF COUP SOURCES

Sequence Number (1)	COUP J (2)	ID(3)	Off. (arcsec) (4)	V (mag) (5)	I (mag) (6)	Spectral Type (7)	A_V (mag) (8)	log T_{eff} (K) (9)	log L_{bol} ($L_\odot$) (10)	R ($R_\odot$) (11)	M ($M_\odot$) (12)	log t (yr) (13)	$\Delta(I-K)$ (mag) (14)	EW(Ca) (Å) (15)	$\langle V \rangle$ (mag) (16)	ΔV (mag) (17)	σ (mag) (18)	P (day) (19)
1..............	053429.4−052337	8	0.39	...	15.73	M5.5	0.00	3.483	−0.98	1.18	0.14	6.16	...	0.0	...	...	...	...
2..............	053429.5−052354	5	4.85	12.01	10.97	K1	0.29	3.708	0.64	2.69	1.98	6.58	0.01	...	...	...	...	...
3..............	053433.9−052211	25	6.43	17.76	15.22	M4.5	0.00	3.500	−0.88	1.21	0.17	5.95	0.52	0.0	...	...	...	...
4..............	053434.9−052507	...	...	...	...	...	...	...	...	...	...	...	...	...	...	...	...	...
5..............	053438.2−052338	...	...	...	...	...	...	...	...	...	...	...	...	...	...	...	...	...
6..............	053438.2−052423	40	0.36	17.37	14.48	M3.5	0.46	3.518	−0.57	1.60	0.27	6.31	0.12	0.0	14.40	0.06	0.16	9.81
7..............	053439.7−052425	45	0.75	11.38	09.89	K1−K4	0.75	3.661	1.19	6.23	2.12	5.55	−0.02	...	...	...	...	...
8..............	053439.8−052456	...	...	...	...	...	...	...	...	...	...	...	...	...	...	...	...	...
9..............	053439.9−052642	46	1.06	12.39	11.12	K0−K3	0.88	3.708	0.73	2.96	2.11	6.49	0.10	...	...	...	...	...
10............	053440.0−052604	48	1.02	20.10	15.50	M6	1.71	3.471	−0.37	2.49	0.18	5.15	−0.69	1.0	...	...	...	...
11............	053440.8−052242	50	0.70	13.40	11.65	K1e−K7	0.42	3.602	0.44	3.46	0.69	5.74	1.37	−14.6	...	...	...	...
12............	053440.8−052639	51	1.36	16.82	14.45	M1.5	0.77	3.555	−0.57	1.35	0.39	6.45	1.05	0.0	...	...	...	...
13............	053440.9−052559	53	1.14	18.65	15.85	M0	2.58	3.580	−0.71	1.02	0.55	6.93	1.13	1.5	...	...	...	...
14............	053441.6−052357	54	0.76	18.85	15.27	M5	0.77	3.494	−0.68	1.57	0.20	6.34	−0.04	0.0	...	...	...	...
15............	053441.7−052652	55	0.94	17.07	14.40	M3	0.31	3.526	−0.60	1.48	0.29	6.33	0.36	1.0	...	...	...	...

NOTES.—See § 10 for descriptions of the columns. Table 9 is available in its entirety in the electronic edition of the *Astrophysical Journal Supplement*. A portion is shown here for guidance regarding its form and content.

Large Telescope, which reaches 5 σ point source limiting magnitudes of approximately 22, 21, and 20 at J_s, H, and K_s, respectively. The seeing is roughly 0″.5–0″.6 FWHM throughout and thus is a good match to the ACIS PSF in this inner crowded region. Its 1204 point sources are astrometrically tied to the 2MASS reference frame with 0″.15 rms accuracy. As the VLT data are saturated for sources brighter than ∼13 mag in all filters, magnitudes for brighter stars were from other wide-field ONC catalogs and high spatial resolution studies of the inner core region as necessary (McCaughrean & Stauffer 1994; H97; Petr et al. 1998; Simon et al. 1999; Lucas & Roche 2000; Luhman et al. 2000; Muench et al. 2002; Schertl et al. 2003; 2MASS). Care was taken to place all of the photometric data on the 2MASS

JHK_s color system as far as possible, resulting in a homogeneous merged catalog covering the brightest OB stars down to candidate (3–5 M_{Jup}) proto–brown dwarfs in this inner region.

For each catalog, we performed automated cross-correlations between COUP and catalog source positions within a search radius of 1″ for COUP source within ≃3′.5 of the field center, and within a search radius of 2″ in the outer regions of the field where the *Chandra* PSF deteriorates. The results of this search are given in Tables 9 and 10.

To evaluate the merits of this automatic procedure, we performed a careful visual examination of each COUP source. In ≃98% of the cases, the identifications are clear and unambiguous. Median offsets between COUP sources and near-infrared

TABLE 10
PROBABLE NEAR-INFRARED COUNTERPARTS OF COUP SOURCES

COUP			JHK_s BANDS							L BAND		
Sequence Number (1)	COUP J (2)	Source (3)	Off. (arcsec) (4)	J (mag) (5)	H (mag) (6)	K_s (mag) (7)	Source Flag (8)	Phot. Flag (9)	Con. Flag (10)	Ref. Flag (11)	Source Number (12)	L (mag) (13)
1............................	053429.4−052337	05342945−0523374	0.04	13.99	13.37	13.09	...	AAA	ccc	...	...	...
2............................	053429.5−052354	05342924−0523567	4.85	10.19	9.78	9.61	...	AAA	000	...	...	...
3............................	053433.9−052211	05343357−0522087	6.25	13.25	12.54	12.17	...	AAA	000	...	...	...
4............................	053434.9−052507	...	...	...	...	...	...	...	...	...	...	...
5............................	053438.2−052338	...	...	...	...	...	...	...	...	...	...	...
6............................	053438.2−052423	05343822−0524236	0.20	12.73	11.95	11.70	...	AAA	0d0	...	...	...
7............................	053439.7−052425	05343976−0524254	0.48	8.85	8.10	7.95	...	AAA	000	...	...	...
8............................	053439.8−052456	...	...	...	...	...	...	...	...	...	...	...
9............................	053439.9−052642	05343988−0526420	0.55	10.22	9.65	9.46	...	AAA	000	...	...	...
10..........................	053440.0−052604	05344000−0526040	0.45	13.33	12.70	12.34	...	AAA	000	...	...	...
11..........................	053440.8−052242	05344086−0522423	0.37	10.53	9.46	8.60	...	AAA	000	...	...	...
12..........................	053440.8−052639	05344081−0526387	0.77	12.68	11.67	11.14	...	AAA	000	...	...	...
13..........................	053440.9−052559	05344093−0526000	0.75	13.79	12.62	11.93	...	AAA	000	...	...	...
14..........................	053441.6−052357	05344162−0523574	0.30	13.28	12.57	12.28	...	AAA	000	...	...	...
15..........................	053441.7−052652	05344171−0526529	0.54	12.54	11.66	11.14	...	AAA	000	...	...	...

NOTES.—See § 10 for descriptions of the columns. Table 10 is available in its entirety in the electronic edition of the *Astrophysical Journal Supplement*. A portion is shown here for guidance regarding its form and content.
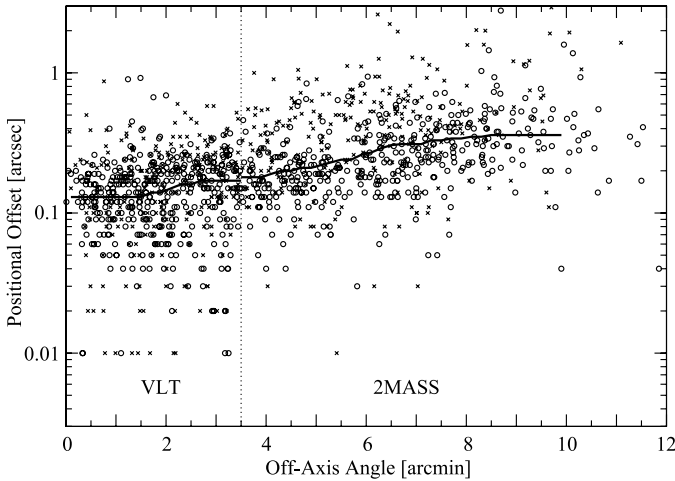
FIG. 9.—Separations between COUP X-ray sources and IR counterparts. For each individual source, symbols present separations between COUP and the VLT catalog within the inner <3.5 region, and COUP and the 2MASS catalog within the outer >3.5 region. Crosses indicate weak X-ray sources with <200 counts, and circles indicate bright X-ray sources with ≥200 counts. Solid lines present the running medians of separations.

stars are only 0″.15, and between COUP and optical stars are only 0″.24[22] indicating superb astrometric positions in the COUP field. Figure 9 shows individual offsets as a function of off-axis angle; median offsets are better than 0″.2 at the central part of the field and 0″.4 at larger off-axis angles. Note that the (unexplained) deterioration of several arcsec in off-axis positions reported by Feigelson et al. (2002a) in earlier Orion ACIS data is not present in COUP positions.

But in a few dozen cases, stellar identifications are complicated due to closely spaced stars, many of which are probably physical binaries. In some cases, a single COUP source spans double NIR and/or optical systems (see notes on individual sources in electronic versions of Tables 9 and 10), while other cases have double COUP sources with a single optical/infrared star. In the former case, the closest optical/IR source is tentatively assigned to a COUP source; in the latter case, either the same optical/infrared counterpart is assigned to two COUP sources (if the 90% PSF contours both encompass the optical/IR position) or an optical/infrared counterpart is tentatively assigned to the closest COUP source. These cases, and other situations where stellar identifications may be insecure, will be discussed separately in Getman et al. (2005). The listings in Tables 9 and 10 are thus probable, and not necessarily confirmed, physical associations between COUP sources and previously identified stars.

In the inner region covered by the deep VLT survey, there are a total of 883 COUP sources detected, 738 of which have stellar counterparts in the McC05 merged catalog. However, that catalog contains a total of 1204 stellar sources in the same region, indicating that the COUP detection rate of cluster members is ∼61%. The great majority of these nonrecovered sources are faint, low-mass members of the cluster, most of which lie in the brown dwarf regime. A careful discussion of the reasons for this fall-off in COUP detections at the lowest masses and their consequences for the X-ray activity of brown dwarfs will be given in a future paper.

We find that 273 (17% of 1616) COUP sources are not identified with any of the known optical/IR sources. Nearly 90% of

these are hard sources with MedE > 2 keV, which is a clear indicator of heavy absorption, and they constitute nearly 40% of all hard COUP sources. However, by itself, this does not determine which of these unidentified sources are new PMS stars associated with the Orion molecular cloud and which are background (primarily extragalactic) sources.

For the probable optical stellar counterparts in Table 9, the star identifier is given in column (3), where designations between 0 and 9999 are from H97 and 10,000–11,000 are from H02. Column (4) gives the offset between the optical and COUP positions. The remaining 15 columns provide optical measurements and inferred stellar properties based largely on the comprehensive study of H97. Columns (5)–(6) give V and I magnitudes from H97. Spectral types in column (7) are from H97, updated with the work of Luhman et al. (2000) and Lucas et al. (2001). Effective temperatures (col. [9]) are based on spectral types following Hillenbrand & White (2004), while visual absorption A_V (col. [8]), bolometric luminosity $\log L_{bol}$ (col. [10]), and radius R (col. [11]) are derived as in H97. Columns (12) and (13) are the mass M and age $\log t$ recalculated by us using the PMS evolutionary tracks of Siess et al. (2000). Users should be cautious when using the intrinsic stellar properties as they are less accurate than the precision given in the tables. Errors arise from intrinsic photometric variability, uncertainties in spectral types and conversions to effective temperatures and bolometric luminosities, and, for the mass and age estimates, uncertainties in theoretical evolutionary tracks (see Hillenbrand & White 2004).

Columns (14)–(15) give two properties associated with circumstellar material and accretion measured by Hillenbrand et al. (1998): the K-band excess attributable to a hot circumstellar disk, $\Delta(I - K)$, and the equivalent width of the Ca II infrared triplet lines with $\lambda = 8542$ Å, EW(Ca). A negative value here represents an emission line. Columns (16)–(19) give properties derived from ∼90 epochs of photometric monitoring by H02: the average V magnitude $\langle V \rangle$ and its standard deviation ΔV, the range in V about this mean, and the rotational period P derived from periodicity attributed to rotationally modulated starspots.

Individual near-infrared counterparts for COUP sources are listed in Table 10 along with infrared properties. Column (3) gives the source identifier obtained from the merged catalog of McC05 for the inner region of the COUP field, and the 2MASS designation for the outer region. The positional offsets and JHK_s magnitudes from the appropriate catalog appear in columns (4)–(7). Column (8) gives a flag for McC05 sources indicating the source of the photometry: 1 from the VLT; 2 and 3 from the New Technology Telescope and Fred Lawrence Whipple Observatory surveys, respectively, presented by Muench et al. (2002); 4 from the compilation of H97, and 5 from 2MASS or other sources. Columns (9)–(10) give flags for 2MASS sources. The values of the photometry quality flag in column (9) are as follows: A, signal-to-noise ratio S/N ≥ 10; B, S/N ≥ 7; C, S/N ≥ 5; D, low-significance detection; E, PSF fitting poor; F, reliable photometric errors not available; X, source detected but no valid photometry is available. The values of the confusion and contamination flag in column (10) are as follows: 0, no problem; b, possible multiple source; c, photometric confusion from nearby star; d, diffraction spike confusion from nearby star; p, persistence contamination from nearby star; and s, electronic stripe from nearby star.

Columns (11)–(13) of Table 10 refer to L-band data. The first column indicates whether the photometry is obtained from the surveys of Muench et al. (2002), designated with an "M," or Lada et al. (2004), designated with an "L." The second column

---

[22] Hillenbrand's positions have been shifted by +0″.78 in right ascension and -0″.38 in declination from the original publication.

TABLE 11

UPPER LIMITS OF UNDETECTED STARS FROM HILLENBRAND (1997)

H97 Number (1)	R.A. (J2000) (deg) (2)	Decl. (J2000) (deg) (3)	LimCt (counts) (4)	Exp. (ks) (5)	Conf. Flag (6)	V (mag) (7)	I (mag) (8)	Spectral Type (9)	A_V (mag) (10)	$\log T_{eff}$ (K) (11)	$\log L_{bol}$ ($L_\odot$) (12)	R ($R_\odot$) (13)	M ($M_\odot$) (14)	$\log t$ (yr) (15)	$\Delta(I-K)$ (mag) (16)	EW(Ca) (Å) (17)
9...............	83.623192	−5.395426	4017	396.2	x	18.94	14.74	K5	8.21	3.695	1.06	4.63	1.61	5.43	...	2.9
23.............	83.639984	−5.385887	67	715.2	...	13.08	12.00	G7	0.82	3.740	0.38	1.71	1.50	6.83	−0.10	...
42.............	83.661568	−5.356926	53	720.7	...	...	16.41	G:	...	...	...	...	...	...	...	4.7
3060..........	83.674896	−5.358895	44	688.1	x	18.60	16.27	...	...	...	...	...	...	...	...	...
3073..........	83.677109	−5.379485	46	746.7	...	...	16.60	...	...	...	...	...	...	...	...	...
62.............	83.678688	−5.421204	55	749.9	...	17.64	14.59	Early-K	5.26	3.695	0.40	2.17	1.38	6.21	−0.10	1.5
67.............	83.682404	−5.424037	53	752.6	...	...	16.62	...	...	...	...	...	...	...	...	...
86.............	83.694984	−5.434676	45	760.4	...	18.64	15.83	...	...	...	...	...	...	...	...	...
85.............	83.695068	−5.358148	130	756.8	x	17.39	14.78	M2.5	0.59	3.535	−0.71	1.25	0.26	6.15	0.14	4.1
108...........	83.708405	−5.312427	66	454.9	x	10.19	9.29	A2−A7	2.07	3.940	2.01	4.46	3.59	...	0.63	...
141...........	83.729233	−5.449654	208	667.4	x	18.27	15.43	G:	...	...	...	...	...	...	...	1.3
179...........	83.741188	−5.478287	237	731.5	x	...	16.65	M5.5	0.00	3.483	−1.34	0.77	0.09	6.32	...	0.0
5084..........	83.754486	−5.340973	24	789.3	...	...	16.99	...	...	...	...	...	...	...	...	...
214...........	83.757027	−5.443426	23	702.6	...	...	16.75	...	...	...	...	...	...	...	...	...
219...........	83.758736	−5.306343	35	765.1	...	19.82	15.52	M5	2.62	3.494	−0.33	2.35	0.15	4.43	0.12	0.3

NOTE.—Table 11 is available in its entirety in the electronic edition of the *Astrophysical Journal Supplement*. A portion is shown here for guidance regarding its form and content.

gives the running source number from the *L*-band catalog. The final column gives the *L* magnitude.

11. NONDETECTIONS OF CLUSTER MEMBERS

Tables 11 and 12 provide lists of upper limits for the H97 $V < 20$ optical catalog and the 2MASS $K < 15$ near-infrared catalog. The first three columns in the tables give object identification name or number and star position from the associated catalog. The next three columns give information from the COUP image: the upper limit on the number of counts at that position, effective exposure time at the object position, and a confusion flag if the object is influenced by nearby sources. The remaining columns reproduce catalog optical and near-infrared properties for the stars (see § 10). We underscore the importance of the contamination and confusion flags in the 2MASS data set, as a

considerable number of 2MASS cataloged sources are small-scale bright spots in the diffuse nebular emission rather than true stars.

The upper limits to the COUP counts for these sources were calculated using PWDetect and are therefore consistent with the PWDetect detection procedure. They indicate the minimum source counts required, for a detection using PWDetect at a significance level of 5.0 σ, i.e., the same used for detection. Our final source list contains some sources with fewer counts than the upper limits derived by PWDetect. This can be due to (1) the use of other detection methods, which can, in some situations, be more sensitive than PWDetect (e.g., the eye is able to detect a faint source close to a bright one more easily than a wavelet based detection algorithm, especially where the PSF is azimuthally distorted); (2) random fluctuations in the spatial distribution

TABLE 12

UPPER LIMITS OF UNDETECTED STARS FROM THE TWO MICRON ALL-SKY SURVEY

2MASS Source (1)	LimCt (counts) (2)	Exp. (ks) (3)	Conf. Flag (4)	J (mag) (5)	H (mag) (6)	K_s (mag) (7)	Phot. Flag (8)	Con. Flag (9)
05342954−0523437	3891	383.9	x	11.90	10.70	10.11	AAA	000
05343297−0522142	475	126.4	...	16.63	15.30	14.60	CUU	c00
05343359−0523099	66	715.2	...	11.28	10.78	10.72	AAA	000
05343419−0524593	615	490.2	...	18.65	16.20	15.13	UCB	000
05343508−0521498	1044	200.6	...	16.95	16.34	15.51	UUC	000
05343646−0521458	454	485.4	...	16.77	15.87	15.16	BBB	000
05343725−0525101	59	729.6	...	16.88	15.60	15.28	CBB	000
05343824−0524024	150	733.4	...	15.96	14.70	14.23	AAA	000
05343850−0523255	132	713.1	x	16.07	14.53	14.06	AAA	000
05343873−0521250	53	719.4	...	14.10	13.05	12.67	AAA	000
05344062−0523150	50	720.5	...	16.14	15.17	14.84	AAA	000
05344065−0526526	657	445.8	x	16.73	16.26	15.44	BCB	ccc
05344135−0524442	58	744.9	...	16.87	15.91	15.50	CCB	ccc
05344196−0521321	44	687.5	...	14.16	13.48	13.12	AAA	000
05344224−0522325	46	745.1	...	16.50	15.14	14.64	BAA	c00

NOTES.—Note that some of these sources are bright spots in the diffuse nebular emission rather than stellar photospheres. Table 12 is available in its entirety in the electronic edition of the *Astrophysical Journal Supplement*. A portion is shown here for guidance regarding its form and content.
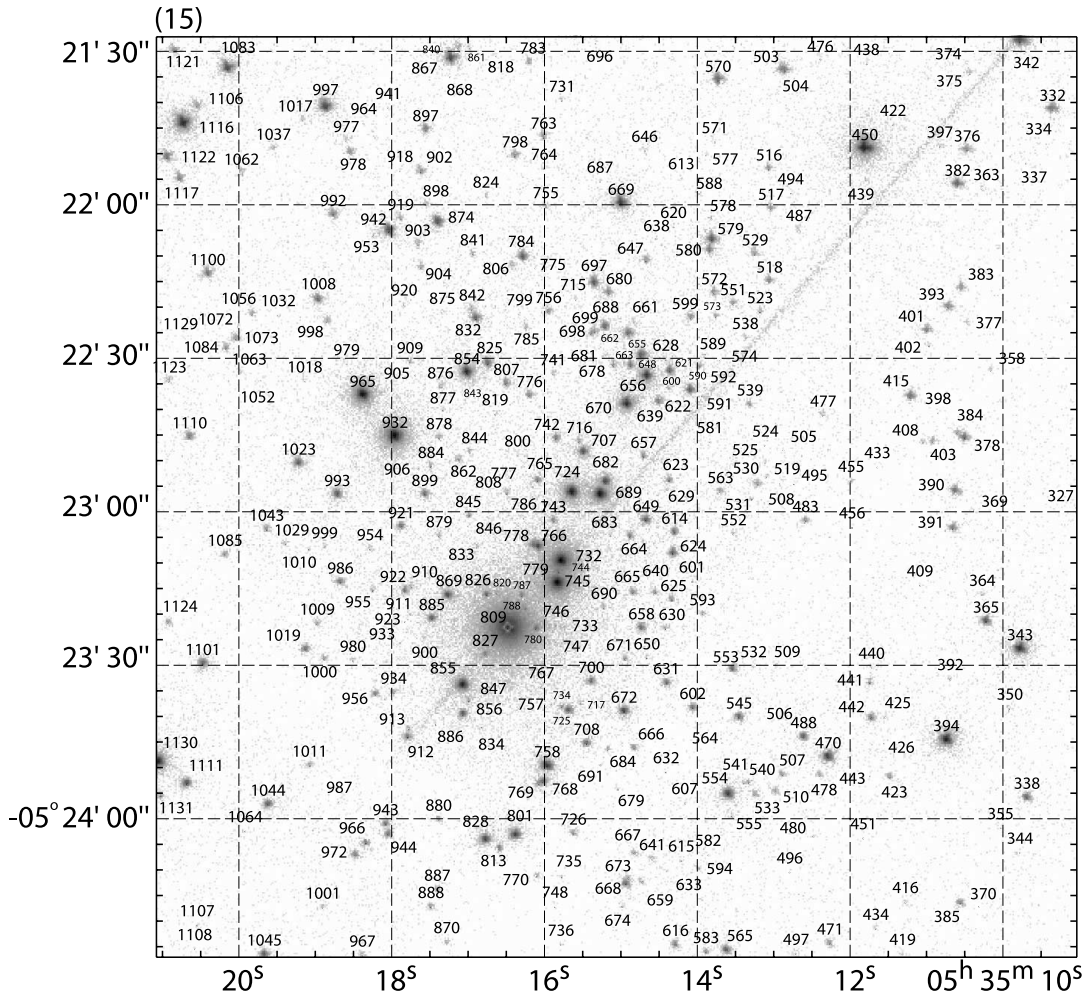
Fig. 10.—Expanded views of the merged COUP ACIS-I data with sources indicated. Panel numbers are indicated in parentheses in the upper left corner of each panel and refer back to Fig. 11.

of source events raising the S/N of a source above the detection threshold. Such a source would be undetectable if it had a nominal PSF.

For most stars, the upper limits are estimated analytically from the source-free background map computed by PWDetect. In many cases where the undetected stars lie on PSF wings of a detected source (as indicated by the flag in Tables 11 and 12), the analytical method may significantly overestimate upper limits. More stringent limits were derived for such sources by adding test sources at a variety of count levels at the upper limit position in the ACIS image. The wavelet transforms of these simulated images were then examined to determine the minimum count level (reported as the upper limit in our tables) at which the simulated source becomes detectable (i.e., produces a second peak next to that of the detected source).

It is often desirable to estimate the luminosity upper limits, and we include a possible procedure below (these luminosity upper limits will be included in a future COUP publication). Derive an upper limit to the count rate as LimCt/Exp using Tables 11 and 12, calculate N_H according to the formula $N_H(\mathrm{cm}^{-2}) \sim A_V(\mathrm{mag})(1.6 \times 10^{21})$ (Vuong et al. 2003), and use PIMMS to compute the unabsorbed flux from the count rates, assuming an optically thin plasma spectrum with $kT \sim 1$ keV. Although the mean temperature of the detected COUP sources is somewhat higher than 1 keV, there is a trend of increasing temperature with increasing X-ray luminosity, and since we can expect the

undetected objects to be more similar to the faintest X-ray sources, 1 keV should be a reasonable value.

12. MAPS AND SOURCE ATLAS

Figure 10 provides close-up maps covering the entire merged COUP ACIS-I field with 1616 COUP sources labeled. The field was divided into 29 panels with the innermost panel having the highest resolution. A guide to the map panels is provided in Figure 11; this guide also gives the pixel size for each panel. The plotted intensities are scaled to the log of the photons in each pixel.

The `acis_extract` package also produces an "atlas" in which both tabulated and graphical information on each source is collected onto a single page. Figure Set 12 in print shows a sample page; see the electronic edition for the full atlas. The graphs display various projections of the four-dimensional ACIS dat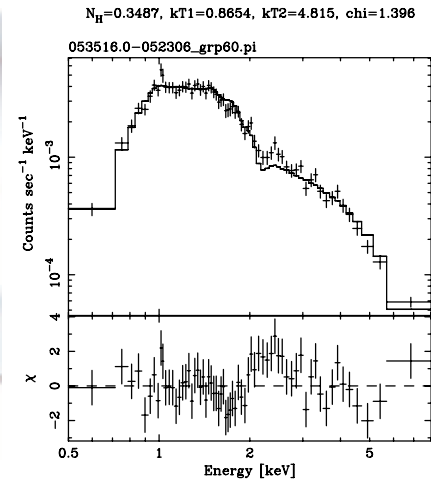a set—photons as a function of R.A., Decl., energy, and time—with ancillary plots associated with our spatial, spectral, and variability analysis.[23]

After the COUP source name, the upper panel of each atlas page shows the light curve of extracted events without background subtraction. In the few cases where the source lies near a gap in the CCD array, it covers only the primary CCD. The

[23] The 1616 pages of the COUP atlas are also available in PDF format at http://www.astro.psu.edu/users/gkosta/COUP/DATA_PRODUCTS_08_17_04/ATLAS/.

FIG. 10.—Continued

(3)

1574
1569
1565 1554
1549
1579
1550
1580
1561
1563
1586
1557
1589
1576
1584
1566
1582
1585
1587
1577
1571

1534
1536 1526 1519
1531
1542 1529
1523
1525
1521
1509
1538 1533
1530
1527
1545 1510

20' 00"
21' 00"
22' 00"
23' 00"
24' 00"
-05°25' 00"

05ʰ 35ᵐ 44ˢ   42ˢ   40ˢ   38ˢ   36ˢ   34ˢ

(4)

1571
1572 1567
1583 1573
1588
1570
1578
1590
1568
1555 1552
1551
1556

1517
1537
1558 1522 1512
1560 1506
1539 1514 1505
1547 1511
1564 1520
1553
1559 1543
1546 1515
1507
1516
1524
1518

26' 00"
27' 00"
28' 00"
29' 00"
30' 00"
-05°31' 00"

05ʰ 35ᵐ 44ˢ   42ˢ   40ˢ   38ˢ   36ˢ   34ˢ

Fɪɢ. 10.—*Continued*

FIG. 10.—*Continued*

Fig. 10.—Continued

(6)

(7)

(8)

(9)

FIG. 10.—*Continued*

F<small>IG</small>. 10.—*Continued*

FIG. 10.—*Continued*

346

F<small>IG</small>. 10.—*Continued*

FIG. 10.—*Continued*

348

(5)
6.5' x 3.2'
0.5" pix

(2)
3' x 3.9'
0.5" pix

(6)
3' x 3'
0.5" pix

(13)
3' x 3'
0.5" pix

(19)
3' x 3'
0.5" pix

(25)
3' x 4.3'
0.5" pix

(1)
4.4' x 9.5'
0.5" pix

(3)
3' x 6'
0.5" pix

(7)
3' x 3'
0.25" pix

(14)
3' x 3'
0.25" pix

(20)
3' x 3'
0.25" pix

(29)
4' x 8.5'
0.5" pix

(8)
3' x 3'
0.25" pix

(15)
3' x 3'
0.125" pix

(21)
3' x 3'
0.25" pix

(26)
3' x 3'
0.5" pix

(9)
3' x 3'
0.25" pix

(16)
3' x 3'
0.25" pix

(22)
3' x 3'
0.25" pix

(27)
3' x 3'
0.5" pix

(4)
3' x 6'
0.5" pix

(10)
3' x 3'
0.5" pix

(17)
3' x 3'
0.5" pix

(23)
3' x 3'
0.5" pix

(28)
3' x 3'
0.5" pix

(11)
3' x 3'
0.5" pix

(18)
3' x 3'
0.5" pix

(24)
4.1' x 3'
0.5" pix

(12)
5.5' x 2.8'
0.5" pix

-05°15'

20'

25'

30'

35'

05ʰ36ᵐ00ˢ   50ˢ   40ˢ   30ˢ   20ˢ   10ˢ   35ᵐ00ˢ   50ˢ   40ˢ   30ˢ

FIG. 11.—Guide to the expanded views of the merged COUP ACIS-I data.

053516.0−052306

N_H=0.3487, kT1=0.8654, kT2=4.815, chi=1.396

053516.0−052306_grp60.pi
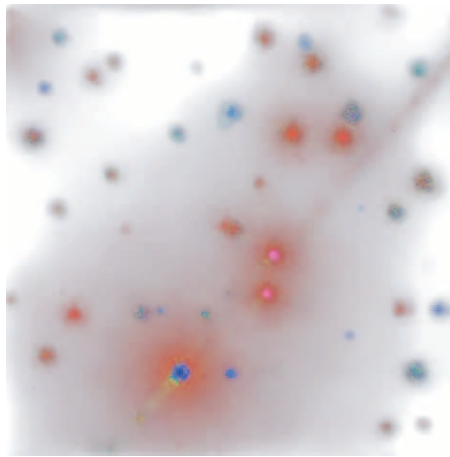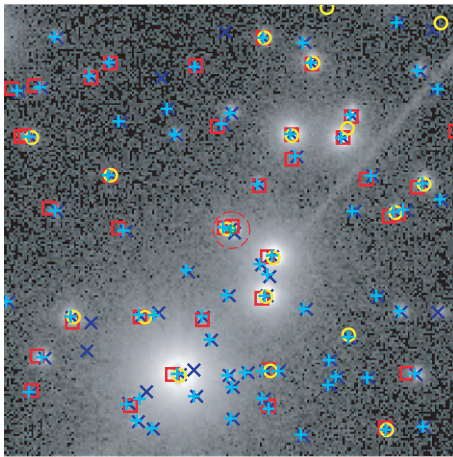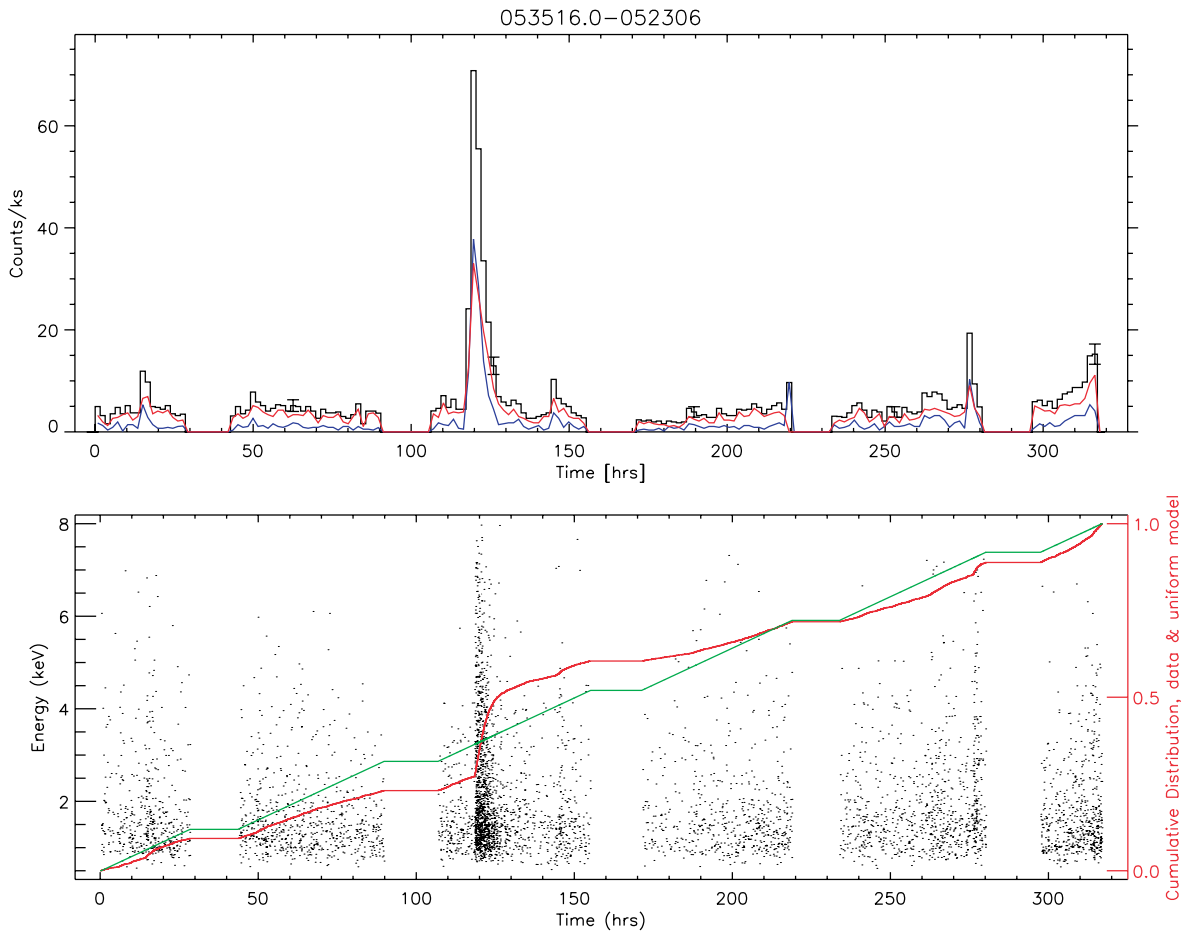
Seq	766	CXOONCJ	053516.0-052306	RA deg	83.817009	DE deg	-5.385267	Offaxis	0.60	ACIS#	519
HRC#	340	JHK-Src	565	JHK-Off	0.09	J	9.74	H	8.37	K s	7.35
Ph-Flg	555	L-RfFlg	M	L-Src	460A	L	5.50	H97-Src	1863b	H97-Off	0.43
H97-V	—	H97-I	11.00	SpTy	—	Av	—	Mass	—	Age	—
NetCts	5091	BkgCts	7	PSFFrac	0.39	ExpTime	832.9	MedEn	1.58	HR1	-0.32
ChipGap	—	logPbK S	-4.0	BB#	20	BBMin	1.76	BBMax	109.45	logNH	21.54
kT1	0.87	kT2	4.82	logEM1	52.83	logEM2	53.52	chi2	1.40	dof	61
logL s	30.07	logL h	30.41	logL h-c	30.42	logL t	30.57	logL t-c	30.71		

Comments:

FIG. SET 12.—Sample page from the COUP source atlas. [*See the electronic edition of the Supplement for Figs. 12.2−12.1616*].

abscissa is in hours from the start of the observation and the ordinate is in counts ks^{-1}. The black histogram shows the total 0.5–8.0 keV energy band, while the red lines show the soft (0.5–2.0 keV) and the blue lines show the hard (2.0–8.0 keV) energy bands. The light curve binning depends on source strength according to the following scheme: SrcCnts < 200, bin width =6.3 hr; <500, 3.2 hr; <10,000, 1.6 hr; <20,000, 1.1 hr; <40,000, 47.6 minutes; and ≥40,000, 23.8 minutes.

The second panel presents the photon arrival times as a function of energy in the total energy band. The overplotted lines represent the cumulative distributions of data (*red*) and uniform model (*green*), used to compute the K-S variability test (§ 8).

The bottom left and center panels show the raw and adaptively smoothed images around the source. The images subtend $50\rlap{.}''5 \times 50\rlap{.}''5$ size with $0\rlap{.}''25$ pixel bins oriented with north at the top and east to the left. Brightness is scaled to the logarithm of counts in each pixel; isolated individual events are always visible in the raw image. The raw image shows a green polygon representing the `acis_extract` source extraction region and a red circle representing the source mask used in construction of the Penn State background map ($1.1 \times 97\%$ PSF region). Small colored symbols indicate the location of IR and optical sources: cyan plus signs are from the VLT *JHK* catalog, yellow circles are from the 2MASS *JHK$_s$* catalog, blue crosses are from the MLLA *JHKL* catalog, and red squares are from the optical catalog of H97. The adaptive smoothing is performed using the CIAO tool `csmooth` at the 2.5 σ level. The adaptively smoothed image in the center panel is a "true-color"[24] X-ray image where red represents the 0.5–1.7 keV band counts, green the 1.7–2.8 keV counts, and blue the 2.8–8.0 keV counts.

The bottom right panel of each atlas page shows the extracted source spectrum after background subtraction and the chosen model from the XSPEC spectral fitting procedure (§ 7 and Table 6). The top plot shows the source spectrum after grouping as separated lines with error bars and a continuous step-function representing the fitted model. The abscissa is in units of log (keV), and the ordinate is in units of log (counts s^{-1} keV^{-1}). The bottom plot shows residuals in units of contribution to the χ^2 statistic.

Finally, below the figures on each page of the COUP atlas we collect many of the X-ray positional, photometric, spectral, variability, and stellar counterpart quantities given in Tables 2–8.

13. SUMMARY

This paper presents the observations, data analysis methodology, and tabulated results for the *Chandra* Orion Ultradeep Project. We describe techniques used in the COUP data reduction, derivation of time-averaged source properties, and production of the source catalog. The results of this study are the tables of the 1616 COUP source properties (Tables 2, 4, 6, 7, 8, 9, and 10), tables of undetected sources (Tables 11 and 12), a map of the field (Fig. 10), and the 1616 page atlas detailing the analysis and findings for each source (Figure Set 12).

---

[24] Red, green, and blue images are scaled using a color model (from the TARA package http://www.astro.psu.edu/xray/docs/TARA/) that preserves the "hue" of the data (ratios among red, green, and blue signals), even for regions where the brightness is saturated. The color white and other shades of gray appear only where the red, green, and blue signals are approximately equal. A similar technique has been described by Lupton et al. (2004).

Our data reduction procedure seeks to use the most well-developed methods available for the identification and extraction of point sources in *Chandra* ACIS images. The source detection procedure is based on two wavelet-based search algorithms, run on data sets constructed in several bands, supplemented by visual inspection of the image. The data set is optimized for maximum reduction of background and maximum spatial resolution with subpixel event repositioning. We identify 1616 X-ray sources in the ∼$17' \times 17'$ ACIS-I field.

For each source, we perform data extraction, pile-up analysis, spectral analysis, variability analysis, and broadband luminosity determinations using the sophisticated semiautomated IDL-based `acis_extract` package. The algorithms used in `acis_extract` successfully address many difficulties related to the COUP observation such as the position-dependent PSF, multiple exposures with different pointings and time gaps, source crowding, piled-up sources, nonuniform local background and exposure map, and so on. Our treatment of photon pile-up for strong sources using annular extraction regions is first used here in a formal procedure. The `acis_extract` package, which is available to the public, can be used to create point source catalogs for many *Chandra* studies.

These images, atlases, and tables serve as the foundation for various studies of the COUP observations. These will include investigation of X-ray emission from different classes of pre–main-sequence stars: OB, intermediate-mass, and T Tauri stars and brown dwarfs; deeply embedded stars, which are often younger protostars; and binary and multiple star systems. We will also investigate the astrophysical issues such as the magnetic field generation and geometries in pre–main-sequence systems, plasma energetics in powerful magnetic reconnection flaring events, and X-ray ionization of circumstellar disks and cloud material. Altogether, the COUP data products presented here offer the most detailed and comprehensive information to date concerning the X-ray emission and magnetic activity in pre–main-sequence stars.

REFERENCES

Alcalá, J. M., et al. 1996, A&AS, 119, 7
Arnaud, K. A. 1996, in ASP Conf. Ser. 101, Data Analysis Software and Systems V, ed. G. H. Jacoby & J. Barnes (San Francisco: ASP), 17
Audard, M., Güdel, M., Sres, A., Raassen, A. J. J., & Mewe, R. 2003, A&A, 398, 1137
Bradt, H. V., & Kelley, R. L. 1979, ApJ, 228, L33

Broos, P. S., Townsley, L. K., & Nousek, J. A. 1998, Proc. SPIE, 3444, 30
Cutri, R. M., et al. 2003, 2MASS All-Sky Catalog of Point Sources (Pasdena: IPAC)
Damiani, F., Maggio, A., Micela, G., & Sciortino, S. 1997a, ApJ, 483, 350
Damiani, F., Maggio, A., Micela, G., & Sciortino, S. 1997b, ApJ, 483, 370
Davis, J. E. 2001, ApJ, 562, 575
den Boggende, A. J. F., Mewe, R., Gronenschild, E. H. B. M., Heise, J., & Grindlay, J. E. 1978, A&A, 62, 1
Feigelson, E. D., Broos, P., Gaffney, J. A., Garmire, G., Hillenbrand, L. A., Pravdo, S. H., Townsley, L., & Tsuboi, Y. 2002a, ApJ, 574, 258
Feigelson, E. D., Gaffney, J. A., Garmire, G., Hillenbrand, L. A., & Townsley, L. 2003, ApJ, 584, 911
Feigelson, E. D., Garmire, G. P., & Pravdo, S. H. 2002b, ApJ, 572, 335
Feigelson, E. D., & Montmerle, T. 1999, ARA&A, 37, 363
Flaccomio, E., Damiani, F., Micela, G., Sciortino, S., Harnden, F. R., Murray, S. S., & Wolk, S. J. 2003a, ApJ, 582, 382
———. 2003b, ApJ, 582, 398
Freeman, P. E., Kashyap, V., Rosner, R., & Lamb, D. Q. 2002, ApJS, 138, 185
Gagné, M., Caillault, J.-P., & Stauffer, J. R. 1995, ApJ, 445, 280
Garmire, G. P., Bautz, M. W., Ford, P. G., Nousek, J. A., & Ricker, G. R. 2003, Proc. SPIE, 4851, 28
Garmire, G., Feigelson, E. D., Broos, P., Hillenbrand, L. A., Pravdo, S. H., Townsley, L., & Tsuboi, Y. 2000, AJ, 120, 1426
Gehrels, N. 1986, ApJ, 303, 336
Geier, S., Wendker, H. J., & Wisotzki, L. 1995, A&A, 299, 39
Getman, K. V., et al. 2005, ApJS, 160, 353
Giacconi, R., Murray, S., Gursky, H., Schreier, E., & Tananbaum, H. 1972, ApJ, 178, 281
Glassgold, A. E., Feigelson, E. D., & Montmerle, T. 2000, in Protostars and Planets IV, ed. V. Mannings, A. P. Boss, & S. S. Russell (Tucson: Univ. Arizona Press), 429
Herbst, W., Bailer-Jones, C. A. L., Mundt, R., Meisenheimer, K., & Wackermann, R. 2002, A&A, 396, 513 (H02)
Hillenbrand, L. A. 1997, AJ, 113, 1733 (H97)
Hillenbrand, L. A., Strom, S. E., Calvet, N., Merrill, K. M., Gatley, I., Makidon, R. B., Meyer, M. R., & Skrutskie, M. F. 1998, AJ, 116, 1816
Hillenbrand, L. A., & White, R. J. 2004, ApJ, 604, 741
Imanishi, K., Koyama, K., & Tsuboi, Y. 2001, ApJ, 557, 747
Kang, H., van Dyk, D. A., Yu, Y., Siemiginowska, A., Connors, A., & Kashyap, V. L. 2003, in Statistical Challenges in Astronomy, ed. E. D. Feigelson & G. J. Babu (New York: Springer), 449

Kastner, J. H., Huenemoerder, D. P., Schulz, N. S., Canizares, C. R., & Weintraub, D. A. 2002, ApJ, 567, 434
Ku, W. H.-M., & Chanan, G. A. 1979, ApJ, 234, L59
Lada, C. J., Muench, A. A., Lada, E. A., & Alves, J. F. 2004, AJ, 128, 1254
Li, J., Kastner, J. H., Prigozhin, G. Y., Schulz, N. S., Feigelson, E. D., & Getman, K. V. 2004, ApJ, 610, 1204
Lucas, P. W., & Roche, P. F. 2000, MNRAS, 314, 858
Lucas, P. W., Roche, P. F., Allard, F., & Hauschildt, P. H. 2001, MNRAS, 326, 695
Luhman, K. L., Rieke, G. H., Young, E. T., Cotera, A. S., Chen, H., Rieke, M. J., Schneider, G., & Thompson, R. I. 2000, ApJ, 540, 1016
Lupton, R., Blanton, M. R., Fekete, G., Hogg, D. W., O'Mullane, W., Szalay, A., & Wherry, N. 2004, PASP, 116, 133
Lyons, L. 1993, Am. J. Phys., 61, 189
Matsumura, S., & Pudritz, R. E. 2003, ApJ, 598, 645
McCaughrean, M. J., & Stauffer, J. R. 1994, AJ, 108, 1382
Mewe, R. 1991, A&A Rev., 3, 127
Morrison, R., & McCammon, D. 1983, ApJ, 270, 119
Muench, A. A., Lada, E. A., Lada, C. J., & Alves, J. 2002, ApJ, 573, 366 (MLLA)
Petr, M. G., Coude Du Foresto, V., Beckwith, S. V. W., Richichi, A., & McCaughrean, M. J. 1998, ApJ, 500, 825
Scargle, J. D. 1998, ApJ, 504, 405
Schertl, D., Balega, Y. Y., Preibisch, T., & Weigelt, G. 2003, A&A, 402, 267
Schulz, N. S., Canizares, C., Huenemoerder, D., Kastner, J. H., Taylor, S. C., & Bergstrom, E. J. 2001, ApJ, 549, 441
Schulz, N. S., Canizares, C. R., Huenemoerder, D., & Lee, J. C. 2000, ApJ, 545, L135
Schulz, N. S., Canizares, C., Huenemoerder, D., & Tibbets, K. 2003, ApJ, 595, 365
Siess, L., Dufour, E., & Forestini, M. 2000, A&A, 358, 593
Simon, M., Close, L. M., & Beck, T. L. 1999, AJ, 117, 1375
Townsley, L. K., Broos, P. S., Nousek, J. A., & Garmire, G. P. 2002, Nucl. Instrum. Meth. Phys. Res. A, 486, 751
Townsley, L. K., Feigelson, E. D., Montmerle, T., Broos, P. S., Chu, Y., & Garmire, G. P. 2003, ApJ, 593, 874
Vuong, M. H., Montmerle, T., Grosso, N., Feigelson, E. D., Verstraete, L., & Ozawa, H. 2003, A&A, 408, 581
Weisskopf, M. C., Brinkman, B., Canizares, C., Garmire, G., Murray, S., & Van Speybroeck, L. P. 2002, PASP, 114, 1
Yamauchi, S., Koyama, K., Sakano, M., & Okada, K. 1996, PASJ, 48, 719